Analysis of loads, motions and cavity dynamics during freefall wedges vertically entering the water surface

Jingbo Wang[a,*], Claudio Lugni[b,a], Odd Magnus Faltinsen[a]

[a]*Centre for Autonomous Marine Operations and Systems (AMOS), Norwegian University of Science and Technology, N-7491 Trondheim, Norway*

[b]*CNR-INSEAN: Italian Research Council - Institute for Marine Technology, Roma, Italy*

Abstract

In this paper, theoretical models are developed and numerical methods are used to analyze the loads, motions and cavity dynamics for freefall wedges with different deadrise angles vertically entering the water surface at Froude numbers: $1 \leq Fn < 9$. The time evolutions of the penetration depth, the velocity and the acceleration are analyzed and expressed explicitly. The maximum and average accelerations are predicted. The theoretical results are compared with numerical data obtained through a single-fluid BEM model with globally satisfactory agreement. The evolution of the pressures on the impact side is investigated. Before flow separation, gravity and the acceleration of the wedge have negligible influence on the pressure on the impact side for large Froude numbers or small deadrise angles; with increasing the deadrise angle or decreasing Froude number, the effects of gravity and the acceleration of the wedge tend to become more important. Global loads, with the main emphasis on the drag coefficient, are also studied. It is found that for the light wedge, the transient drag coefficient has slow variation in the first half of the collapse stage and rapid variation in the last half of the collapse stage. For the heavy wedge, the transient drag coefficients vary slowly during the whole collapse stage and can be treated as constant. The characteristics of the transient cavity during its formation are investigated. The non-dimensional pinch-off time, pinch-off depth and submergence depth at pinch-off scale roughly linearly as the Froude number.

Keywords: *wedge; water entry; loads; motions; cavity dynamics*

1. Introduction

When a freefall wedge vertically enters the water surface, it may experience slamming, transition, collapse, and post-closure stages [1]. The slamming stage is the initial stage of the wedge penetrating the water surface. During this stage, the water rises up, jets are formed at the body sides and impulse loads may occur. By impulse loads we mean that the local pressures on the impact side (the side contacting the water) of the wedge and the global vertical load acting on the wedge is impulsive in time. The pressure distribution on the impact side is also spatially 'impulsive' with a localised region of high pressure. The magnitude of the impulse loads and the pressure distribution on the impact side are also of interest. By assuming a constant entry speed and neglecting the effect of the gravity, Dobrovol'skaya [2] presented similarity solutions for the water entry of a wedge with any deadrise angle β. The similarity solution is not available in explicit form and numerical results were only presented for $\beta \geq 30^{\circ}$. Zhao & Faltinsen [3] developed advanced numerical methods and presented numerical results for deadrise angles from 4° to 81°. Zhao and Faltinsen concluded: when $\beta \geq 45^{\circ}$, the maximum pressure is at the apex of the wedge; when β is less than 30° approximately, high impulse pressures are concentrated on a small area near the root of the jet. Carcaterra *et al.* [4, 5] developed analytical models for the hydrodynamic force and wedge motion during the slamming stage, which assumes a constant

---

* Corresponding author. Tel: +47 95978375. E-mail address: jingbo.wang@hotmail.com

entry speed and neglects gravity force. During the water entry of freefall wedges, both gravity force and wedge acceleration influence the wedge motion and/or the hydrodynamic force. For a low-speed water entry, the gravity force is comparable to or even larger than the hydrodynamic force and therefore have an important influence on the wedge motion; for a high-speed water entry, the freefall wedge experiences large vertical accelerations and therefore the added mass force becomes important. In the present paper, the effects of gravity and accelerations are taken into account. Special attention is given on how gravity and the vertical acceleration influence the pressures on the impact side of the wedge. When the jet reaches the knuckle of the wedge, non-viscous flow separation occurs. The jet breaks up into spray. When the root of the jet/spray leaves the knuckle of the wedge, a strong drop of the slamming force occurs and the transition stage starts. It is interesting how the pressures on the impact evolve during the transition stage. When the root of the spray is far away from the knuckle, an open cavity is formed on the top of the wedge which then collapses. The collapse stage ends at closure (pinch-off) of the cavity during which the hydrodynamic loads change slowly [1]. The evolution of the global hydrodynamic loads, the wedge motions and the evolution of the cavity are of particular interest. Wang & Faltinsen [6] investigated the evolution of the cavity numerically showing that: the cavity closure period is independent of the initial entry speed of the wedge; the submergence depth of the wedge at pinch-off increases approximately linearly with respect to the initial entry speed; and the cavity size is highly dependent on the mass with a larger mass causing a larger cavity. Here, we will discuss the mechanics behind these numerical findings.

In this paper, theoretical models are developed to describe the wedge motions and cavity dynamics of a freefall wedge vertically entering the water surface. The present study is focused on the kinematics and dynamics of the freefall wedge until the closure of the cavity. No consideration is given to the post-closure stage where air compressibility matters [1]. The time evolutions of the penetration depth, the velocity and the acceleration are analyzed and expressed explicitly. The maximum and average accelerations of the wedge are predicted. The theoretical analyses show the existence of a critical Froude number: for Froude number less than the critical Froude number the velocity of the wedge increases after the slamming stage; for Froude number larger than the critical Froude number the velocity decreases after the slamming stage. This is accordance with Wang et $al.$´s experiments [1]. An approximate cavity evolution model is proposed. The non-dimensional pinch-off time of the cavity scales linearly as the Froude number. Further, the characteristics of the transient cavity are predicted and it is found that the non-dimensional pinch-off depth and submergence depth (the distance from the still water level to the top side of the wedge) at pinch-off scale roughly linearly as the Froude number. The evolution of the pressures on the impact side and the drag coefficients are also extensively studied. It is found that for the light wedge the transient drag coefficients (see Eq. (21)) have slow variation in the first half of the collapse stage and rapid variation in the last half of the collapse stage; for the heavy wedge the transient drag coefficients vary slowly during the whole stage and can be treated as constant. Note that the numerical results presented in this paper are obtained by using the single-fluid BEM described in [1].

2.   Loads and motions

A two-dimensional wedge with mass M, deadrise angle β, beam $2c_0$ vertically impacts the still water surface with initial entry speed V_0 as shown in Fig. 1. The surface tension σ can be neglected provided that the Weber number $W = \rho V_0^2 c_0 / \sigma \gg 1$. Viscous effects may be excluded within the short duration of the impact and for high Reynolds number $Re = \rho V_0 c_0 / \mu$. Further, we neglect the influence

of the air flow. This assumption is in accordance with the study of Wang *et al.* [1]: for closure of 2D cavity, the air flow starts to play an important role just before the closure but its influence is very limited. Then the impact is characterized by the Froude number $Fn = V_0/\sqrt{gc_0}$, the mass ratio, and the deadrise angle β. Here, the mass ratio could be defined as the hydrostatic mass ratio $D_1 = \rho c_0 h_0/M$ or the hydrodynamic mass ratio $D_2 = 0.5\rho\pi c_0^2/M$. The hydrostatic mass ratio is the ratio between the mass of water displaced by the fully-submerged wedge and the mass of the wedge, and the hydrodynamic mass ratio is the ratio between the added mass of the wedge (the high frequency added mass of a flat plate approximation is $0.5\rho\pi c_0^2$) and the mass of the wedge. The latter is more suitable to represent the mass ratio since the water impact is a dynamic process.

2.1 Global load and wedge motion

2.1.1 Slamming stage and transition stage

During the slamming stage, the water rises up due to the impact of the wedge, and jets are formed at the body sides as shown in Fig. 1. The penetration depth of the wedge satisfies

$$\frac{dh}{dt} = V .\tag{1}$$

Based on the conservation of fluid momentum, the slamming force (see page 299 in [7]) can be expressed as

$$-\frac{d}{dt}(A_{33}V) .$$

Here A_{33} is the vertical added mass of the wedge, which can be represented as $A_{33} = 0.5\rho\pi c^2$. c is regarded as the equivalent half-wetted breadth and can be expressed as a water rise-up ratio λ times the measurement on the still water surface, i.e.

$$c = \lambda(h/\tan\beta).\tag{2}$$

Note that $\lambda = \pi/2$ corresponds to Wagner's approach [8] and $\lambda = 1$ von Kármán's approach [9]. If the Wagner-Sydow approximation [10] is used, the water rise-up ratio may be written as

$$\lambda = (\pi/2\beta - 1)tan\beta.\tag{3}$$

Further, by neglecting the buoyancy and following Newton's second law the equation of motion of the wedge can be expressed as

$$M\frac{dV}{dt} = -\frac{d}{dt}(A_{33}V) + Mg .\tag{4}$$

We define the following non-dimensional variables: $\tilde{t} = t/\tau_0$, $\tilde{h} = h/c_0$, $\tilde{c} = c/c_0$, and $\tilde{V} = V/V_0$. Here $\tau_0 = c_0/V_0$. The equations of motion of the wedge are written in non-dimensional form as

$$\frac{d\tilde{h}}{d\tilde{t}} = \tilde{V}\tag{5}$$

and

$$\frac{d\tilde{V}}{d\tilde{t}} = -D_2\frac{d}{d\tilde{t}}(\tilde{c}^2\,\tilde{V}) + \frac{1}{Fn^2} .\tag{6}$$

Integrating (6) from 0 to $\tilde{t}$ yields

$$\tilde{V} = \frac{1}{1+D_2\tilde{c}^2}(1+\frac{1}{Fn^2}\tilde{t}) .\tag{7}$$

From (6), we can get

$$\frac{d\tilde{V}}{d\tilde{t}} = -\frac{2D_2\tilde{c}\lambda\tan^{-1}(\beta)\tilde{V}^2}{1+D_2\tilde{c}^2} + \frac{1}{1+D_2\tilde{c}^2}\frac{1}{Fn^2} .\tag{8}$$

Substituting (7) into (5) and integrating from 0 to $\tilde{t}$, the following relation between $\tilde{c}$ and $\tilde{t}$ is obtained

$$\left(\tilde{c}+\frac{1}{3}D_2\tilde{c}^3\right)\lambda^{-1}\tan\beta = \tilde{t}+\frac{\tilde{t}^2}{2Fn^2}.\tag{9}$$

When the root of the jet reaches the knuckle of the wedge, the slamming stage ends and the transition stage starts. This can be regarded to occur at $\tilde{c}=1$. The corresponding time $\tilde{t}_*$ can be expressed as

$$\tilde{t}_* = Fn^2\left(-1+\sqrt{1+\frac{2\tan\beta}{Fn^2}\lambda^{-1}(1+\frac{D_2}{3})}\right),$$

(10)

when the velocity of the wedge is

$$\tilde{V}_* = \frac{1}{1+D_2}\sqrt{1+\frac{2\tan\beta}{Fn^2}\lambda^{-1}(1+\frac{D_2}{3})}.\tag{11}$$

The acceleration of the wedge at $\tilde{t}_*$ corresponds to the peak acceleration

$$\tilde{a}_{peak} = -\frac{2D_2\lambda\tan^{-1}(\beta)\tilde{V}_*^2}{1+D_2}+\frac{1}{1+D_2}\frac{1}{Fn^2}.\tag{12}$$

Due to flow separation, the slamming force drops dramatically during the transition stage. Neglecting the rate of change of the half-wetted breadth at this stage, Eq. (6) becomes

$$\frac{d\tilde{V}}{d\tilde{t}} = \frac{1}{1+D_2}\frac{1}{Fn^2}.\tag{13}$$

It can be shown that, when the wedge reaches $h=h_0$, its velocity becomes

$$\tilde{V}_1 = \frac{1}{1+D_2}\sqrt{1+\frac{2\tan\beta}{Fn^2}\left[1+(1-\lambda^{-1}\frac{2}{3})D_2\right]}.\tag{14}$$

Based on Eqs. (12) and (14), we can conclude that:

(i) A wedge with small mass ($D_2 \gg 1$) results in $\tilde{V}_1 \approx 0$, i.e. after the impact its velocity is significantly reduced.

(ii) A small deadrise angle β means that $\tan\beta$ is small and D_2 may be large. It also implies $\tilde{V}_1 \approx 0$.

(iii) A high speed impact, i.e. $Fn \gg 1$, results in

$$\tilde{V}_1 \approx 1/(1+D_2)\tag{15}$$

and

$$\tilde{a}_{peak} \approx -\frac{2D_2}{(1+D_2)^3}\frac{\lambda}{\tan\beta}.\tag{16}$$

The dimensional form,

$$a_{peak} = -\frac{2D_2}{(1+D_2)^3}\frac{\lambda}{\tan\beta}Fn^2g,\tag{17}$$

shows the peak value of the acceleration grows quadratically with respect to Fn.

When $\beta \to 0$, the water rise-up ratio λ under the approximation of (3) becomes $\pi/2$, which is consistent with the Wagner's [8] inner flow solution; when $\beta \to \pi/4$, it becomes 1, which corresponds to no water rise-up assumption [9]; when $\beta > \pi/4$, it becomes less than 1, which is inconsistent with physics. Eq. (3) shows that the water rise-up ratio λ decreases with increasing the deadrise angle. For $\beta > \pi/4$, no water rise-up approximation, i.e. $\lambda = 1$ could be safely used.

Assuming no water rise-up, the high-frequency added mass of the wedge with the deadrise angle $\beta > \pi/4$ can be expressed as an added mass coefficient times the high-frequency added mass of the flat plate [11]

$$A_{33} = k_{33} \frac{1}{2} \rho \pi c^2 \tag{18}$$

with

$$k_{33} = \frac{1}{\pi} \left[\frac{\Gamma(3/2 - \beta/\pi)\Gamma(\beta/\pi)}{\Gamma(\beta/\pi + 1/2)\Gamma(1 - \beta/\pi)} - 1 \right] \frac{\sin 2\beta}{\cos^2 \beta} . \tag{19}$$

Here, Γ denotes Gamma function. Then, the mass ratio should be modified as

$$D_2^* = k_{33} D_2 \tag{20}$$

The modified mass ratio is more suitable to characterize the impact for the deadrise angle larger than $\pi/4$. By setting $\lambda = 1$ and replacing D_2 with D_2^*, Eqs. (9)-(17) are still valid under the no water rise-up assumption.

Fig. 2 compares the theoretically predicted $\tilde{V}_1$ with the numerical results (of the single-fluid BEM [1]) and good agreements are obtained. Fig. 3 compares the theoretically predicted peak accelerations with the numerical results (of the single-fluid BEM [1]). The theoretical values agree with the numerical simulations except for the case corresponding to the light wedge with deadrise angle $\beta = 30$ $^{\circ}$, for which the theoretical model underestimates the numerical result by 16% for large Froude numbers. Note that no peak acceleration occurs when a freefall wedge with a large deadrise angle enters the water surface at low speed.

2.1.2 Collapse stage

The coordinate system used for the collapse stage is shown in Fig. 4.

For a floating body, the classical technique decomposes the hydrodynamic force acting on the floater into added mass force, wave damping, restoring force and other components. However, this technique can not be applied to the water entry of a freefall object because during water entry, a cavity may be formed on the top of the object. The cavity significantly influences the hydrodynamic coefficients of the falling object, which are essentially transient. This suggests the need for more suitable methods to describe the motion of the wedge. For a sphere, Lee *et al.* [12] describe the deceleration equation as

$$M \frac{dV}{dt} = Mg - \underbrace{0.5 \rho V^2 C_D^* 2c_0}_{F_d^*} . \tag{21}$$

Here F_d^* denotes the drag force，and C_D^* denotes the drag coefficient. C_D^* is typically taken to be constant for subsonic water entry [12,13]. Then the question is raised: how does the drag coefficient behave for the water entry of a freefall wedge. By denoting t_z as the time when the top of the wedge reaches z, we introduce $\bar{t} = (t - t_z)/\tau_0$ and $\bar{t}_{pinch}$ the pinch-off time of the cavity. Fig. 5 shows the time evolution of C_D^* for a light and a heavy freefall wedge with deadrise angle $\beta = 30^{\circ}$ as predicted numerically by using single-fluid BEM [1]. For the light wedge, the drag coefficient C_D^* varies slowly for approximately up to the half of the pinch-off time and during this period it can be taken to be constant; from the half of the pinch-off time until the pinch-off occurs, C_D^* grows rapidly and obviously cannot be treated as constant. For the heavy wedge, C_D^* varies slowly during the whole collapse stage and it can be safely taken to be constant. Note that the drag coefficient C_D^* for freefall wedges with

other deadrise angles has similar behaviors. Fig. 6 shows the mean drag coefficient $\bar{C}_D^*$, which is obtained by averaging C_D^* over the first half of the collapse stage. It can be seen that the mean drag coefficient decreases by increasing the Froude number or deadrise angle and is weakly dependent on the mass ratio. The following equations represent the fitting of numerical mean drag coefficients for $D_2 = 1/6$:

$$\begin{aligned}\bar{C}_D^* = {}& 3.4412 - 1.2738 Fn + 3.9159 \times 10^{-1} Fn^2 - 7.5198 \times 10^{-2} Fn^3 \\ & + 8.7112 \times 10^{-3} Fn^4 - 5.5594 \times 10^{-4} Fn^5 + 1.4985 \times 10^{-5} Fn^6 \end{aligned} \qquad \text{for} \quad \beta = 30° \qquad (22.a)$$

$$\begin{aligned}\bar{C}_D^* = {}& 2.8878 - 0.86795 Fn + 2.0779 \times 10^{-1} Fn^2 - 2.8769 \times 10^{-2} Fn^3 \\ & + 2.1192 \times 10^{-3} Fn^4 - 6.4198 \times 10^{-4} Fn^5 \end{aligned} \qquad \text{for} \quad \beta = 40° \qquad (22.b)$$

$$\begin{aligned}\bar{C}_D^* = {}& 2.4269 - 0.62201 Fn + 1.2017 \times 10^{-1} Fn^2 - 1.2532 \times 10^{-2} Fn^3 \\ & + 0.62892 \times 10^{-3} Fn^4 - 1.0637 \times 10^{-5} Fn^5 \end{aligned} \qquad \text{for} \quad \beta = 50° \qquad (22.c)$$

$$\begin{aligned}\bar{C}_D^* = {}& 2.0176 - 0.45667 Fn + 0.71632 \times 10^{-1} Fn^2 - 0.55431 \times 10^{-2} Fn^3 \\ & + 0.16663 \times 10^{-3} Fn^4 \end{aligned} \qquad \text{for} \quad \beta = 60° \qquad (22.d)$$

These equations are valid for $0.5 < Fn < 9$ and can be used as an approximation for other mass ratios (since the mean drag coefficient is weakly dependent on the mass ratio). Eq. (21) is used to study the motion of the wedge during the first half of the collapse stage. Its dimensionless form is

$$\frac{d\bar{V}}{d\bar{t}} + \frac{2}{\pi} \bar{C}_D^* D_2 \bar{V}^2 = \frac{1}{Fn^2} . \qquad (23)$$

By defining the critical speed $\bar{V}_C = \sqrt{\pi / (2\bar{C}_D^* D_2 Fn^2)}$, the solution of Eq. (23) can be expressed as

$$\bar{V} = \bar{V}_C \frac{(\bar{V}_1 + \bar{V}_C)e^{\frac{4}{\pi}\bar{V}_C \bar{C}_D^* D_2 \bar{t}} + (\bar{V}_1 - \bar{V}_C)}{(\bar{V}_1 + \bar{V}_C)e^{\frac{4}{\pi}\bar{V}_C \bar{C}_D^* D_2 \bar{t}} - (\bar{V}_1 - \bar{V}_C)} . \qquad (24)$$

Here, $\bar{V}_1 \equiv \tilde{V}_1$. Eq. (24) shows that $\bar{V} \to \bar{V}_C$ when $\bar{t} \to \infty$. If $\bar{V}_1$ is smaller than $\bar{V}_C$, the velocity of the body will monotonically increase to the critical speed; if $\bar{V}_1$ is larger than $\bar{V}_C$, the velocity of the body will monotonically decrease to the critical speed. This indicates that there exists a critical Froude number Fn_{cr}: if the Froude number is less than the critical Froude number, the velocity of the wedge will increase during the first half of the collapse stage; if the Froude number is larger than the critical Froude number, the velocity of the wedge will decrease during the first half of the collapse stage. Using Eq. (14), the critical Froude number is approximated as

$$Fn_{Cr} = \sqrt{\frac{\pi}{2} \frac{(1 + D_2)^2}{\bar{C}_D^* D_2} - 2\left(1 + (1 - \lambda^{-1}\frac{2}{3})D_2\right) \tan \beta} . \qquad (25)$$

From Wang *et al.* (2014)'s [1] experiments, the critical Froude number is calculated to be 1.4. The experimental and numerical results shown in Fig. 7 confirm the above analysis.

Integrating expression (24) with respect to time, we will get the expression of the submergence depth (see Fig. 4), i.e.

$$\bar{H} = -\bar{V}_C \bar{t} + \frac{\pi}{2\bar{C}_D^* D_2} \ln \left[\frac{(\bar{V}_C + \bar{V}_1)e^{\frac{4}{\pi}\bar{V}_C \bar{C}_D^* D_2 \bar{t}} + (\bar{V}_C - \bar{V}_1)}{2\bar{V}_C} \right] . \qquad (26)$$

Fig. 8 illustrates the submergence depth and the velocity predicted by Eqs. (24) and (26) and compared against the numerical results (of the single-fluid BEM [1]).

Inserting $d\overline{V}/d\overline{t} = \overline{V}d\overline{V}/d\overline{H}$ into Eq. (23) and solving the transformed equation, we obtain:

$$\overline{V}^2 = \overline{V}_C^2 + \left[\overline{V}_1^2 - \overline{V}_C^2\right]e^{-\frac{4}{\pi}D_2\overline{C}_D^*\overline{H}} .$$ (27)

Differentiating expression (27) with respect to time, gives the acceleration:

$$\frac{d\overline{V}}{d\overline{t}} = -\frac{2}{\pi}D_2\overline{C}_D^*\left[\overline{V}_1^2 - \overline{V}_C^2\right]e^{-\frac{4}{\pi}D_2\overline{C}_D^*\overline{H}} .$$ (28)

Thus, the average acceleration over the whole collapse stage is

$$\Lambda = \frac{1}{\overline{H}_{pinch}}\int_0^{\overline{H}_{pinch}}\frac{d\overline{V}}{d\overline{t}}d\overline{H} = \frac{1}{2\overline{H}_{pinch}}\left[\overline{V}_1^2 - \overline{V}_C^2\right](e^{-\frac{4}{\pi}D_2\overline{C}_D^*\overline{H}_{pinch}} - 1) .$$ (29)

Here, $\overline{H}_{pinch}$ denotes the submergence depth at the pinch-off as shown in Fig. 4. The average acceleration over the first half of the pinch-off time is

$$\Lambda_{1/2} = \frac{1}{\overline{H}_{1/2}}\int_0^{\overline{H}_{pinch}}\frac{d\overline{V}}{d\overline{t}}d\overline{H} = \frac{1}{2\overline{H}_{1/2}}\left[\overline{V}_1^2 - \overline{V}_C^2\right](e^{-\frac{4}{\pi}D_2\overline{C}_D^*\overline{H}_{1/2}} - 1) .$$ (30)

Here, $\overline{H}_{1/2} \equiv \overline{H}(\overline{t} = 0.5\overline{t}_{pinch})$.

Figs. 9-10 compare the theoretical predictions of Λ and $\Lambda_{1/2}$ with the corresponding numerical results (of the single-fluid BEM [1]). In general, the theoretical predictions of $\Lambda_{1/2}$ are in a satisfactory agreement with the numerical results. For the cases corresponding to light wedges with low Froude numbers, discrepancy between the theoretical result and the numerical result are observed. The discrepancy increases with increasing the deadrise angle and can reach 0.06 for the case corresponding to $\beta = 30^o$ and $Fn = 1$. Eq. (29) can well predict Λ of heavy wedges but fails in predicting Λ of light wedges with low Froude numbers. This is not surprising; according to the results of Fig. 5 the drag coefficient C_D^* of the light wedge varies dramatically with respect to time during the last half of the collapse stage and it cannot be assumed constant. The rapid variation of C_D^* for the light wedge during the last half of the collapse stage occurs because the hydrostatic component of the drag force becomes dominant. This increases the difficulties for a reliable theoretical model. To get slowly-varying drag coefficients, one must include the hydrostatic force in the definition of the drag coefficient as follows [14, 15]

$$C_D^{**} = \frac{F_d^*}{\rho V^2 c_0 + \rho g H 2 c_0} .$$ (31)

Figs. 11 illustrate the time evolutions of C_D^{**} for a freefall wedge with deadrise angle $\beta = 30^o$ vertically entering into water. By including the hydrostatic force, C_D^{**} also for the light wedge varies slowly during the last half of the collapse stage and therefore can be taken to be constant. Note that the drag coefficient C_D^{**} for freefall wedges with other deadrise angles has similar behaviors.

Fig. 12 shows the mean value, $\overline{C}_D^{**}$, of C_D^{**} over the last half of the collapse stage by numerical simulations. The mean drag coefficient $\overline{C}_D^{**}$ decreases with increasing the Froude number and is weakly dependent on the mass ratio and the deadrise angle. The following equations represent the fitting of numerical mean drag coefficients (obtained by using the single-fluid BEM [1]) for $D_2 = 1/6$:

$$\begin{aligned}\overline{C}_D^{**} &= 0.9347 - 1.3437\times10^{-1}Fn + 2.202\times10^{-2}Fn^2 - 2.0006\times10^{-3}Fn^3 \\ &\quad + 7.3756\times10^{-5}Fn^4\end{aligned} \qquad \text{for } \beta = 30^o$$ (32.a)

$$\overline{C}_D^{**} = 0.8849 - 1.1242 \times 10^{-1} Fn + 1.5825 \times 10^{-2} Fn^2 - 1.2213 \times 10^{-3} Fn^3$$
$$+ 3.8229 \times 10^{-5} Fn^4 \qquad \text{for} \quad \beta = 40° \qquad (32.b)$$

$$\overline{C}_D^{**} = 0.83774 - 0.96671 \times 10^{-1} Fn + 1.1735 \times 10^{-2} Fn^2 - 0.74929 \times 10^{-3} Fn^3$$
$$+ 1.8423 \times 10^{-5} Fn^4 \qquad \text{for} \quad \beta = 50° \qquad (32.c)$$

$$\overline{C}_D^{**} = 0.79754 - 0.85221 \times 10^{-1} Fn + 0.79959 \times 10^{-2} Fn^2 - 0.25432 \times 10^{-3} Fn^3$$
$$- 0.4472 \times 10^{-5} Fn^4 \qquad \text{for} \quad \beta = 60° \qquad (32.d)$$

These equations are valid for $0.5 < Fn < 9$ and can be used as an approximation for other mass ratios. Under the new definition of the drag coefficient, the deceleration of the wedge becomes

$$\frac{d\overline{V}}{d\overline{t}} + \frac{2}{\pi} \overline{C}_D^{**} D_2 \left(\overline{V}^2 + \frac{2\overline{H}}{Fn^2} \right) = \frac{1}{Fn^2} . \qquad (33)$$

This equation can be solved numerically, for instance using a Runge-Kutta method. Eq. (23) is used to describe the deceleration of the wedge for the first half of the collapse stage and Eq. (33) for the last half of the collapse stage. The solution of Eq. (23) matches that of Eq. (33) when

$$\frac{2}{\pi} \overline{C}_D^* D_2 \overline{V}^2 = \frac{2}{\pi} \overline{C}_D^{**} D_2 \left(\overline{V}^2 + 2\overline{H} / Fn^2 \right)$$

is satisfied. Fig. 13 compares the time evolutions of the submergence depth and the velocity for the light wedge entering the water. By matching Eq. (23) with Eq. (33), the theoretical predictions have been significantly improved especially for the evolution of the velocity.

2.2 Pressure evolution

Zhao & Faltinsen [3] investigated the water entry of the wedge with constant entry speed in a zero-gravity environment before flow separation. They concluded: (i) when $\beta \geq 45°$, the maximum pressure is at the apex of the wedge; (ii) when β is less than $30°$ approximately, high impulse pressures are concentrated on a small area near the root of the jet. In this section, we use the single-fluid model [1, 6] to investigate the evolution of the pressures on the impact side before and after flow separation, which takes into account the effect of gravity and the acceleration of the wedge. Fig. 14 illustrates the evolution of the pressure and free surface on the impact side before flow separation for the water entry of a freefall wedge with a deadrise angle of $30°$, $D_2 = 1/3$, and $Fn=1$. At the jet the pressure is very close to atmospheric pressure; a peak pressure occurs at the root of the jet; towards the apex of the wedge, the pressure decreases and tends to be flat. Such a pressure distribution is similar to the water entry of a wedge with constant speed in a zero-gravity environment [16, 3]. Fig. 15 compares the numerical results of the single-fluid model with the similarity solution [3] for the peak pressure coefficient ($Cp_{max} = P_{max}/(0.5\rho V^2)$) on the impact side before the flow separation: the numerical peak pressure coefficient is about 6.8, which is quite close to the value of 6.9 predicted by the similarity solution.

Fig. 16 illustrates the evolution of the free surface and the pressure distribution on the impact side during the slamming, transition and collapse stages. When the jet reaches the knuckle of the wedge, non-viscous flow separation occurs. The jet breaks up into spray. However, since the pressure in the jet or in the spray is almost equal to the atmospheric pressure, the jet or the spray does not influence the overall flow and the pressure distribution along the impact side. When the root of jet is close to the knuckle of the wedge, the peak pressure starts to vanish and the transition stage starts. When the root of the spray is away from the knuckle, the pressure distribution on the impact side is changed to a new

configuration (the pressure varies strongly around the knuckle point and the maximum pressure is at the apex of the wedge) and the transition stage is ended. During the collapse stage, the maximum pressure on the impact side may grow with increasing the penetration depth of the wedge.

Fig. 17 illustrates the evolution of the pressure on the impact side before flow separation for the water entry of a freefall wedge with a deadrise angle of 60° and $D_2 = 1/3$. The peak pressure occurs at the apex of the wedge. When the initial entry speed is relatively small, the pressure distribution on the impact side is significantly different from the similarity solution. It indicates that gravity and/or the acceleration of the wedge play an important role. For relatively large entry speeds, the pressure distribution on the impact side is close to the similarity solution. This is not surprising since a larger Froude number ($Fn = V_0/\sqrt{gc_0}$) the effect of gravity less important. Fig. 18 shows the coefficients of the peak pressure (at the apex) against Froude number, which confirms that the pressure tends to the similarity solution with increasing Froude number. So far, we may conclude that during the water entry of a freefall wedge with a relatively small deadrise angle, gravity and the acceleration of the wedge have a negligible influence on the pressure distribution on the impact side of the wedge before flow separation and the pressure distribution on the impact side is close to the similarity solution. With increasing the deadrise angle or decreasing the initial entry speed, the effects of gravity and/or the acceleration of the wedge tend to become more important.

3. Cavity dynamics

The cavity dynamics of an object entering liquid surfaces have been investigated since the beginning of the 20th century. Worthington (1908) [17] discovered the cavity which follows the vertical entry of spheres into water, and he discussed qualitatively the splash, surface seal of the cavity and many other details of the cavity history. Gilbarg & Anderson [18] studied the influence of the atmospheric pressure on the phenomena accompanying the water entry of spheres. Their experiments showed that surface sealing of the cavity is a major factor in controlling cavity formation and is the factor most responsible for non-Froude scaling of cavity phenomena, and they concluded surface sealing is a function mainly of the atmospheric density and projectile velocity. After their work, May [19] carried out more detailed studies. He investigated experimentally several parameters (such as the density and pressure of the atmosphere, and the velocity and size of the sphere) on the time and place of occurrence of various events in the life of the cavity. Lee *et al.* [12] studied the cavity formation and collapse induced by high-speed impact and penetration of a rigid projectile into water. Duclaux *et al.* [20] proposed a theoretical model to describe the cavity dynamics of the sphere entering into water for 'low Froude numbers'. They approximated the near field flow (close to the cavity wall) as a 2D source flow and neglected the far field flow. The near field region is determined to be $R < r < R_\infty \approx 2.7R$ by an assumed energy relationship (here, R is the radius of the cavity wall). Then they derived an equation for the cavity dynamics, based on which the characteristics of the cavity such as the cavity depth and the time at pinching were analysed. Note that the Duclaux *et al.* ´s model assumes a constant water entry speed. Aristoff *et al.* [21] studied the effect of deceleration on the cavity dynamics during the water entry of spheres. First, they established the equations of motions of spheres by assuming a constant form drag coefficient. Then based on the Duclaux's approximate expression for the evolution of the cavity surface, Aristoff discussed the cavity dynamics in detail. Glasheen & McMahon [15] performed an experimental study on vertical water entry of disks at low Froude numbers. They found a linear relationship between the cavity seal depth and the square root of the Froude number. In contrast, the cavity seal time is nearly independent of velocity. It has a linear

relationship with the square root of the radius of disks. Later, Gaudet [14] performed the numerical simulation of disks entering the free surface from very low to moderate Froude numbers. He confirmed some parameter relationships found by Glasheen and McMahon [15], discussed the effects of the dimensionless disk mass on the cavity dynamics and found a bifurcation in the cavity seal mechanism from deep seal to surface seal at the critical Froude number, $V_0^2/gR_0 = 105$ (R_0 is the radius of disk). Recently, Bergmann *et al.* [22] studied the cavity dynamics for vertical water entry of disks with constant speed. They presented a free-parameter model and concluded that the closure depth and total depth of the cavity are both roughly dependent on the square root of the Froude number and gave the scaling of the entrained bubble volume. These works about the cavity dynamics are related to the water entry of spheres or disks and most of the works assumed constant entry speeds. Further, the theoretical models for the water entry of freefall objects did not take into account the effects of slamming stage(after this stage, the velocity of the falling objects may be significantly changed), and assumed constant drag coefficients (which may be not suitable for the falling objects with relatively small mass). Wang & Faltinsen [23, 4] investigated the evolution of the cavity during a freefall wedge vertically entering the water surface. They developed numerical methods and found: the cavity closure period is independent of the initial entry speed of the wedge; the submergence depth of wedge at pinch-off increases approximately linearly with respect to the initial entry speed; the cavity size is highly dependent on the mass and a larger mass leads to a larger cavity. In this section, we generalize Duclaux *et al.* ´s approach [20] from the three-dimensional water entry of spheres to the two-dimensional water entry of freefall wedges and develop a theoretical model to describe the cavity dynamics for the water entry of a freefall wedge. In our model, we include the far-field flow, which is neglected by Duclaux *et al.* [20] and seems to be the dominant flow for the water entry of freefall wedges. Based on the proposed cavity model, the pinch-off time $\bar{t}_{pinch}$ and the characteristics of the transient cavity, i.e. the pinch-off depth $\bar{z}_{pinch}$ (see Fig. 4) and the submergence depth at pinch-off $\bar{H}_{pin}$ are investigated and the physics behind the numerical findings [6] are discussed.

Due to the short duration of the impact and the high Reynolds number (for instance, the Reynolds number corresponding to the water entry of a wedge with c_0=0.1m at Fn=1 is approximately 10^6), viscous effects may be excluded. Euler equations are suitable to describe the flow. By assuming that the lateral (horizontal) flow velocity component is much larger than the vertical flow velocity component (this assumption is used by Duclaux *et al.*[20] for investigating the water entry of sphere and by Bergmann *et al.* [22] for the water entry of disk), we neglect the latter and its derivative in the Euler equations and reduce the problem to the equation of the lateral velocity

$$\frac{\partial u}{\partial t} + u\frac{\partial u}{\partial r} = -\frac{1}{\rho}\frac{\partial p}{\partial r} . \tag{34}$$

Here, r is the lateral coordinate as defined in Fig. 4. The problem can be solved by matching a near-field and far-field flow behavior. Based on the conservation of fluid mass, the flow behaves like a source in the region near the cavity surface. Therefore, at the near field the velocity of the fluid can be approximated by the expansion or contraction speed of interface, i.e.

$$u = \dot{R} .$$

At large distance from the cavity surface, velocity should vanish. This means that we can express the velocity in terms of a power series of $1/r$. Keeping the two lowest order terms, the far field solution of the horizontal velocity is approximated as

$$u = C_1\frac{1}{r} + C_2\frac{1}{r^2} . \tag{35}$$

The first term on the right hand side of expression (35) will lead to infinite fluid momentum,

$$\int_R^\infty \frac{1}{r} dr = \infty ,$$

and therefore should vanish. The complete solution is obtained by matching the near field solution with the far field solution at some distance, i.e.

$$u = \begin{cases} \dot{R}, R < r < R_1 \\ (R_1 / r)^2 \dot{R}, r > R_1 \end{cases} .$$

(36)

If Declaux et al' s theory [20] is applied to 2D water entry, the lateral velocity of water is expressed as

$$u = \begin{cases} \dot{R}, R < r < 3R \\ 0, r > 3R \end{cases}$$

Let us investigate the lateral velocity profile during a freefall wedge entering the water surface. The parameters of the freefall wedge corresponds to the case 2 of Wang et al' s experiments [1]. By using the single-fluid BEM [1], we have the numerical distribution of u at the pinch-off depth along the r-axis, which is shown in Fig. 19. During the expansion of the cavity (see the black solid line), the near field behavior is observed. However, as the increasing of y, it quickly exhibits the far field behavior. During the contraction of the cavity (see the red solid line), it is difficult to observe the near-field behavior. It seems that our approximation of the lateral velocity is better than Declaux et al' s approximation .

Integrating Eq. (34) from R to infinity and using expression (36) yields

$$\ddot{R}(2R_1 - R) + 2\dot{R}_1\dot{R} - \frac{\dot{R}}{2} = -gz .$$

(37)

R_1 can be expressed as $R_1 = \eta R$. η may be called as 'thickness ratio of near-field flow region'. It depends on the impact parameters, time and the vertical coordinate z. For simplicity, we assume η constant during the evolution of the cavity. As a consequence, (37) becomes

$$R\ddot{R} + \frac{4\eta - 1}{2(2\eta - 1)} \dot{R}^2 = \frac{-gz}{(2\eta - 1)} .$$

(38)

Introducing $\bar{R} = R/c_0$ and $\bar{z} = z/c_0$, we get the non-dimensional form of Eq. (38)

$$\frac{d\bar{\dot{R}}^2}{\bar{\dot{R}}^2 + \frac{2}{4\eta - 1}\frac{\bar{z}}{Fn^2}} = -\frac{4\eta - 1}{2\eta - 1}\frac{d\bar{R}}{\bar{R}} .$$

(39)

Here $\bar{\dot{R}} = d\bar{R} / d\bar{t}$ denotes the non-dimensional lateral velocity. Eq. (39) can be integrated once to obtain the lateral velocity.

$$\bar{\dot{R}}^2 = -\frac{2}{4\eta - 1}\frac{\bar{z}}{Fn^2} + (\bar{\dot{R}}_0^2 + \frac{2}{4\eta - 1}\frac{\bar{z}}{Fn^2})\left(\frac{\bar{R}_0}{\bar{R}}\right)^{\frac{4\eta - 1}{2\eta - 1}} .$$

(40)

Here $\bar{R}_0 = 1$ and $\bar{\dot{R}}_0 = \bar{\dot{R}}(\bar{t} = 0)$ are the initial conditions. Let

$$A = \frac{2}{4\eta - 1}\frac{\bar{z}}{Fn^2} \quad \text{and} \quad C = 1 + \frac{\bar{\dot{R}}_0^2}{A} .$$

Expression (40) can be rewritten as

$$\bar{R}^2 = A[-1 + C(\bar{R}_0 / \bar{R})^{\frac{4\eta-1}{2\eta-1}}].$$ (41)

At the initial stage, the water is pushed aside by the wedge and the cavity expands. The lateral velocity decreases with increasing the lateral breadth of the cavity. When $\dot{\bar{R}}$ decreases to zero, the maximum lateral breadth of the cavity is obtained, i.e.

$$\bar{R}_{max} = C^{\frac{2\eta-1}{4\eta-1}}.$$ (42)

At the maximum lateral breadth, the expansion stops and the cavity starts to contract. To obtain the analytical solution of Eq. (41), we perform the transformation $\bar{R} = \chi^\nu$ with $\nu = (4\eta - 2)/(8\eta - 3)$. Then Eq. (41) becomes

$$\frac{\sqrt{A}}{\nu} d\bar{t} = \frac{d\chi}{\sqrt{C - \chi^{(8\eta-2)/(8\eta-3)}}}.$$ (43)

Integrating Eq. (43) once and transforming χ back to $\bar{R}$, we obtain the analytical expression of the $\bar{t} \sim \bar{R}$ relationship

$$\bar{t} = \frac{\nu}{\sqrt{AC}} \left\{ \bar{R}^{1/\nu} {}_2F_1\left(\left[\frac{1}{2}, \frac{(8\eta-3)}{(8\eta-2)}\right], \left[\frac{(16\eta-5)}{(8\eta-2)}\right], \bar{R}^{\frac{(4\eta-1)}{(2\eta-1)}} / C\right) \right.$$
$$\left. - {}_2F_1\left(\left[\frac{1}{2}, \frac{(8\eta-3)}{(8\eta-2)}\right], \left[\frac{(16\eta-5)}{(8\eta-2)}\right], 1/C\right) \right\}.$$ (44)

Here $_2F_1$ represents the hypergeometric function. The duration for the cavity expansion is

$$\Delta\bar{t}_{expa} = \frac{\nu}{\sqrt{AC}} \left\{ C^{\frac{(8\eta-3)}{(8\eta-2)}} {}_2F_1\left(\left[\frac{1}{2}, \frac{(8\eta-3)}{(8\eta-2)}\right], \left[\frac{(16\eta-5)}{(8\eta-2)}\right], 1\right) \right.$$
$$\left. - {}_2F_1\left(\left[\frac{1}{2}, \frac{(8\eta-3)}{(8\eta-2)}\right], \left[\frac{(16\eta-5)}{(8\eta-2)}\right], 1/C\right) \right\}.$$ (45)

The cavity takes the same time to contract from the maximum lateral breadth position to the initial position, i.e. the contraction time is $\Delta\bar{t}_{ctra1} = \Delta\bar{t}_{expa}$. Then the contracting cavity accelerates towards the singularity. This stage lasts $\Delta\bar{t}_{ctra2}$, which is expressed as

$$\Delta\bar{t}_{ctra2} = \frac{\nu}{\sqrt{AC}} {}_2F_1\left(\left[\frac{1}{2}, \frac{(8\eta-3)}{(8\eta-2)}\right], \left[\frac{(16\eta-5)}{(8\eta-2)}\right], 1/C\right).$$ (46)

The total survival time $\Delta\bar{t}_s$ of the cavity is

$$\Delta\bar{t}_s = \Delta\bar{t}_{expa} + \Delta\bar{t}_{ctra1} + \Delta\bar{t}_{ctra2} = \frac{\nu}{\sqrt{AC}} \left\{ 2C^{\frac{(8\eta-3)}{(8\eta-2)}} {}_2F_1\left(\left[\frac{1}{2}, \frac{(8\eta-3)}{(8\eta-2)}\right], \left[\frac{(16\eta-5)}{(8\eta-2)}\right], 1\right) \right.$$
$$\left. - {}_2F_1\left(\left[\frac{1}{2}, \frac{(8\eta-3)}{(8\eta-2)}\right], \left[\frac{(16\eta-5)}{(8\eta-2)}\right], 1/C\right) \right\}.$$ (47)

To determine the evolution of the cavity, we need to know the parameter η and the initial expansion velocity $\dot{R}_0$. The Froude number Fn, the deadrise angle β and the mass ratio D_2 can influence the value of η. Besides, η depends on the time and the vertical coordinate z so it is difficult to give a theoretical formula a $\eta(> 1)$. We assume $\eta = 1$ which means that the inner flow is

neglected. For the initial expansion velocity $\dot{R}_0$, a common assumption [20-22] is that $\dot{R}_0$ is proportional to its downward velocity, i.e.

$$\dot{R}_0 = \sigma V \quad \text{or} \quad \overline{\dot{R}}_0 = \sigma \overline{V} .$$ (48)

For the water entry of the wedge, numerical simulations (by using the single-fluid BEM [1]) found that σ is transient but varies slowly during the collapse stage. It is strongly influenced by the deadrise angle, and is also (weakly) influenced by the Froude number and the mass ratio.

Now, we estimate the pinch-off time of the open cavity during the wedge entering into water. In general C is much larger than unity and therefore can be approximated by

$$C \approx \overline{\dot{R}}_0^2 / A .$$

As a consequence, the total survival time of the cavity can be approximated by

$$\Delta \overline{t}_s \approx 2\nu \frac{\overline{R}_0}{A} \, _2F_1\left(\left[\frac{1}{2}, \frac{(8\eta - 3)}{(8\eta - 2)}\right], \left[\frac{(16\eta - 5)}{(8\eta - 2)}\right], 1\right) .$$ (49)

Here $\beta = (8\eta - 3)/(8\eta - 2) \approx 1$ has been used. The pinch-off time is the minimum time over depths $0 < \bar{z} < \infty$ of the cavity collapse,

$$\overline{t}_{pinch} = \min_{0 < \bar{z} < \infty} \{\Delta \overline{t}_s(\bar{z}) + \overline{t}_z\} .$$

Here, $\overline{t}_z \equiv (t_z - t_{z=0})/\tau_0$. By assuming the constant acceleration Λ, we have $\overline{V} = \overline{V}_1 + \Lambda \overline{t}_z$ and $\bar{z} = \overline{V}_1 \overline{t}_z + \frac{1}{2}\Lambda \overline{t}_z^2$. Here, $\overline{V}_1 = \tilde{V}_1$. Therefore, the pinch-off time at a given depth $\bar{z}$ can be expressed by

$$\Delta \overline{t}_s(z) + \overline{t}_z = \frac{1}{\overline{t}_z}\left[\frac{\overline{V}_1 + \Lambda \overline{t}_z}{\overline{V}_1 + 1/2\Lambda \overline{t}_z}\right]\sigma f^2(\eta)Fn^2 + \overline{t}_z .$$ (50)

with

$$f(\eta) \equiv \sqrt{\frac{2(2\eta - 1)(4\eta - 1)}{8\eta - 3} \, _2F_1\left(\left[\frac{1}{2}, \frac{(8\eta - 3)}{(8\eta - 2)}\right], \left[\frac{(16\eta - 5)}{(8\eta - 2)}\right], 1\right)} .$$

$\overline{t}_z$, corresponding to the pinch-off, is the root of

$$\partial(\Delta \overline{t}_s(z) + \overline{t}_z) / \partial \overline{t}_z = 0$$

and is denoted by $\overline{t}_z^{pinch}$. Then its first-order solution with respect to Λ is

$$\overline{t}_z^{pinch} = \sigma^{1/2} f(\eta)Fn .$$ (51)

It is noted that the coefficient of Λ is zero, that is, the first-order solution coincides with the zero-order solution. Substituting expression (51) back into Eq. (50), we obtain the pinch-off time

$$\overline{t}_{pinch} = \sigma^{1/2} f(\eta)Fn\left(1 + \frac{\overline{V}_1 + \Lambda \overline{t}_z}{\overline{V}_1 + 1/2\Lambda \overline{t}_z}\right) \approx 2\sigma^{1/2} f(\eta)Fn .$$ (52)

Here the acceleration Λ has been discussed in the previous section and is a small parameter. Thus

$$\frac{\overline{V_1} + \Lambda \overline{t_z}}{\overline{V_1} + 1/2\Lambda \overline{t_z}}$$

is approximated to unity. The dimensional pinch-off time is therefore estimated as

$$t_{pinch} \approx 2\sigma^{1/2} f(\eta) Fn^* \tau_0 = 2\sigma^{1/2} f(\eta) \sqrt{\frac{c_0}{g}} \, .$$

It is almost independent of the initial entry speed V_0. This is consistent with the numerical finding by Wang & Faltinsen [6]. Further, the length of the cavity at pinch-off is calculated by

$$\int_{\overline{t_z}^{pinch}}^{\overline{t}_{pinch}} \overline{V} d\overline{t} \, .$$

As shown in Fig. 2 and Fig. 9, a larger mass of the wedge leads to larger $\overline{V_1}$ and Λ and therefore larger $\overline{V}$. This explains why a larger mass of the wedge leads to a larger cavity at pinch-off.

Fig. 20 illustrates the comparison of $\overline{t_z}^{pinch}$ and $\overline{t}_{pinch}$ between the numerical results (of the single-fluid BEM [1]) and theoretical results for deadrise angle 30°. It is noted that the value of σ is estimated as 1.25 (for deadrise angle 30° the numerical experiments show σ varies within [1 1.5] during most of the collapse stage). The theoretical results does not include the effect of the mass ratio, but can be regarded as an approximation. The mass of the wedge has significant influence on $\overline{t_z}^{pinch}$ and $\overline{t}_{pinch}$ for high Froude number. It is noted that the use of $\eta = 1$ may underestimate $\overline{t_z}^{pinch}$ and $\overline{t}_{pinch}$.

Fig. 21 shows the numerical results of $\overline{t_z}^{pinch}$ and $\overline{t}_{pinch}$ for the mass ratios $D_2 = 1/3$ and $1/12$ and confirm that the deadrise angle has a negligible influence on the pinch-off time, as found by Wang & Faltinsen [6]. The solid lines denote a linear least-squares fitting of the numerical results , which can be expressed as

$$\overline{t_z}^{pinch} = 1.6707 * Fn - 0.80554 \qquad \text{for} \quad D_2 = 1/3 \tag{53.a}$$

$$\overline{t_z}^{pinch} = 1.8016 * Fn - 1.1617 \qquad \text{for} \quad D_2 = 1/6 \tag{53.b}$$

$$\overline{t_z}^{pinch} = 1.8636 * Fn - 1.3465 \qquad \text{for} \quad D_2 = 1/9 \tag{53.c}$$

$$\overline{t_z}^{pinch} = 1.8957 * Fn - 1.4589 \qquad \text{for} \quad D_2 = 1/12 \tag{53.d}$$

and

$$\overline{t}_{pinch} = 3.3690 * Fn - 0.61837 \qquad \text{for} \quad D_2 = 1/3 \tag{54.a}$$

$$\overline{t}_{pinch} = 3.7988 * Fn - 0.99858 \qquad \text{for} \quad D_2 = 1/6 \tag{54.b}$$

$$\overline{t}_{pinch} = 4.0571 * Fn - 1.3062 \qquad \text{for} \quad D_2 = 1/9 \tag{54.c}$$

$$\overline{t}_{pinch} = 4.2320 * Fn - 1.5455 \qquad \text{for} \quad D_2 = 1/12 \tag{54.d}$$

Eqs. (53) and (54) are valid for $2<Fn<9$ and cover a wide range of mass ratio. For very light wedges ($D_2>2$ approximately), the open cavity will not close [23, 6] and it is meaningless to discuss $\bar{t}_z^{pinch}$ and $\bar{t}_{pinch}$. For $1/3<D_2<2$, Eqs. (53.a) and (54.a) could be used as an approximation. For $1/12<D_2<1/3$, interpolation may give a good approximation. $D_2>1/12$ correspond to very heavy wedges (the mass of the wedge is over 12 times the added mass by a flat-plate approximation) and such wedges are seldom be encountered in ocean engineering contexts.

Now, we can express the pinch-off depth

$$\bar{z}_{pinch} = \bar{H}(\bar{t} = \bar{t}_z^{pinch}),$$ (55)

and the submergence depth at pinch-off

$$\bar{H}_{pinch} = \bar{H}(\bar{t} = \bar{t}_{pinch}).$$ (56)

Figs. (22)-(23) compare the theoretical results predicted by Eqs. (55)-(56) with numerical results (of the single-fluid BEM [1]). Satisfactory agreement is documented. The pinch-off depth $\bar{z}_{pinch}$ and the submergence depth at pinch-off $\bar{H}_{pin}$ increase roughly linearly with respect to Fn. Both $\bar{z}_{pin}$ and $\bar{H}_{pinc}$ increase with decreasing the mass ratio of wedge.

4. Conclusion

Theoretical models are developed and numerical methods (the single-fluid BEM [1]) are used to analyze the loads, motions and cavity dynamics for freefall wedges with different deadrise angles (30°, 40°, 50° and 60°) vertically entering the water surface at Froude numbers: $1 \leq Fn < 9$. Analytical expressions for the time evolutions of the penetration depth, the velocity and the acceleration are derived. The slamming stage, related to the rapid change of the wetted beam, will significantly reduce the velocity of the wedge with small deadrise angle and/or small wedge mass. The wedge velocity after the slamming stage is theoretically predicted and shows very good agreement with the results obtained by numerical simulations. The peak accelerations are also predicted and in general show good agreement with the numerical simulations (for the light wedge with the deadrise angle of 30°, the theoretical model gives slightly underestimated prediction compared to the numerical simulations). With increasing Froude number both the velocity after the slamming stage and the peak acceleration tend to be a constant depending on the mass ratio. There exists a critical Froude number: for Froude number less than the critical Froude number the velocity of the wedge is increasing after slamming stage; for Froude number larger than the critical Froude number the velocity is decreasing after slamming stage. The evolution of the pressures on the impact side is investigated. Before flow separation, gravity and acceleration of the wedge have negligible influence on the pressures on the impact side for large Froude number or small deadrise angles and the pressure distribution is similar to similarity solution; by increasing the deadrise angle or decreasing Froude number, the effects of gravity and the acceleration of the wedge tend to become more important. After flow separation, the pressure distribution on the impact side will be changed, the pressure varies strongly around the knuckle point and the maximum pressure occurs at the apex of the wedge. The transient drag coefficients during the collapse stage of the cavity are extensively studied. It is found that for the light wedge, the transient drag coefficients have slow variation in the first half of the collapse stage and rapid variation in the last half of the collapse stage, due to the dominant effect of the hydrostatic term in the drag force. For the

heavy wedge, the transient drag coefficients vary slowly during the whole stage and can be treated as a constant. By assuming one-dimensional lateral flow and constant near field thickness ratio and neglecting higher-order terms in the far-field solution representing the flow behavior far from the cavity, a cavity model is established. The cavity closure period is independent of the initial entry speed of the wedge and a larger mass leads to a larger cavity. The characteristics of the transient cavity are investigated and it is found that the non-dimensional pinch-off time, pinch-off depth and submergence depth at pinch-off scale roughly linearly as the Froude number and they increase with decreasing the mass ratio.

References

[1]   Wang J, Lugni C, Faltinsen OM. Experimental and numerical investigation of freefall wedges vertically entering the water surface. Submitted to this journal, 2014.

[2]   Dobrovol' skaya ZN. On some problems of similarity flow of fluid with a free surface. J. Fluid Mech. 1969;36: 805-29.

[3]   Zhao R, Faltinsen OM . Water entry of two-dimensional bodies. J. Fluid Mech. 1993; 246: 593-612.

[4]   Carcaterra A, Ciappi E, Iafrati A, Campana EF. Shock spectral analysis of elastic systems impacting on the water surface. J. Sound Vib. 2000; 229: 579-605.

[5]   Carcaterra A, Ciappi E. Hydrodynamic shock of elastic structures impacting on the water: theory and experiments. J. Sound Vib. 2004; 271: 411-439.

[6]   Wang J, Faltinsen OM. Numerical Investigation for Air Cavity Formation During the High Speed Water Entry of Wedges. J. Offshore Mech. Arct. 2013; 135: n1.

[7]   Faltinsen OM. Sea Loads on Ships and Offshore Structures. Cambridge: Cambridge University Press; 1990.

[8]   Wagner H. Über Stoss- und Gleitvogänge an der Oberfläche von Flüssigkeiten. Z. Angew. Math. Mech. 1932;12: 193-235.

[9]   Von Kármán T. The impact of seaplane floats during landing. NACA Tech. Note 321, Washington DC, 1929.

[10] Pierson JD. On the Virtual Mass of Water Associated with an Immersing Wedge. J. Aeronaut. Sci. 1951; 18: 430-31.

[11] Korotkin AI. Added Masses of Ship Structures. Springer Science & Business Media; 2008.

[12] Lee M, Longoria RG, Wilson DE. Cavity dynamics in high-speed water entry. Phys. Fluids 1997: 9: 540.

[13] Charters AC and Thomas RN. The Aerodynamic Performance of Small Spheres from Subsonic to High Supersonic Velocities, J. Aeronaut. Sci. 1945;12: 468-76.

[14] Gaudet S. Numerical simulation of circular disks entering the free surface of a fluid. Phys. Fluids 1998; 10: 2489.

[15] Glasheen JW, McMahon TA. Vertical water entry of disks at low Froude numbers. Phys. Fluids 1996; 8: 2078.

[16] Greenhow M. Wedge entry into initially calm water. Appl.Ocean Res. 1987; 9(4): 214-23.

[17]   Worthington AM. A Study of Splashes. New York: Longmans Green and Company; 1908.

[18]   Gilbarg D. Anderson RA. Influence of atmospheric pressure on the phenomena accompanying the entry of spheres into water. J. Appl. Phys. 1948; 19: 127-39.

[19]   May A. Vertical entry of missiles into water. J. Appl. Phys. 1952; 23: 1362-72.

[20]   Duclaux V, Caillé F, Duez C, Ybert C, Bocquet L, Clanet C. Dynamics of transient cavities. J. Fluid Mech. 2007; 591: 1-19.

[21]   Aristoff JM, Truscott TT, Techet AH, Bush WM. The water entry of decelerating spheres. Phys. Fluids 2010; 22: 032102.

[22]   Bergmann R, Meer D van der, Gekle S, Bos A van der, Lohse D. Controlled impact of a disk on a water surface: Cavity dynamics. J. Fluid Mech. 2009; 633: 381-409.

[23]   Wang J, Faltinsen OM. Numerical Investigation for Air Cavity Formation During the High Speed Water Entry of Wedges. In: Proceedings of the 29th International Conference on Ocean, Offshore and Arctic Engineering, OMAE 2010-20237, Shanghai, China, 2010.

Figures
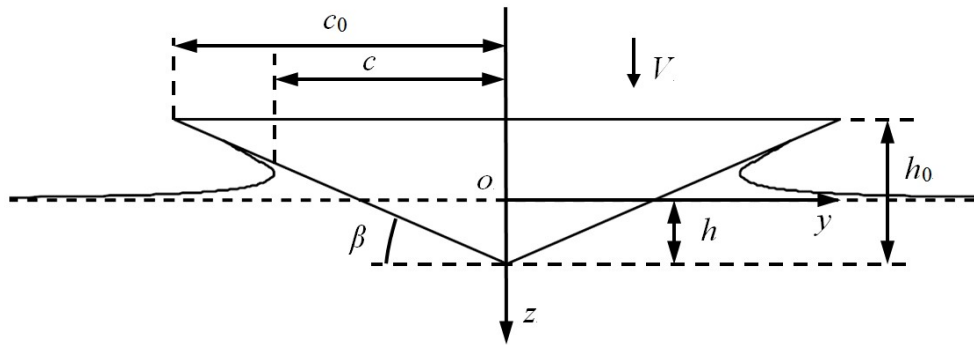
Fig. 1. Coordinate system and symbol definitions for the slamming stage.

a) $\beta = 30°$

b) $\beta = 40°$

c) $\beta = 50°$

d) $\beta = 60°$
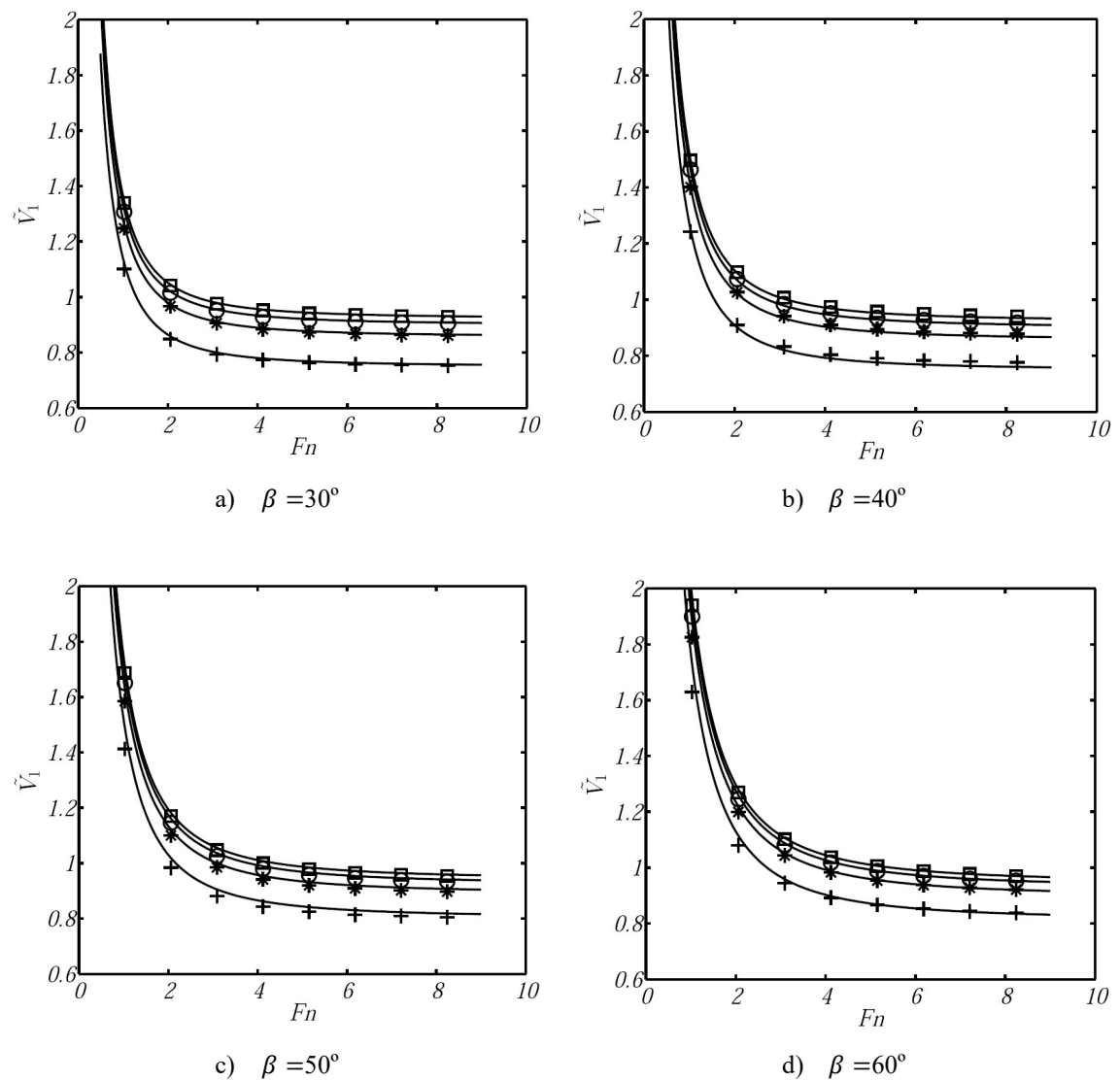
Fig. 2. The velocity of the wedge when $h = h_0$. The solid lines denote the theoretical predictions. Symbols denote the numerical solution. The results refer to different mass ratios: +, $D_2 = 1/3$; *, $D_2 = 1/6$; O, $D_2 = 1/9$; □, $D_2 = 1/12$.
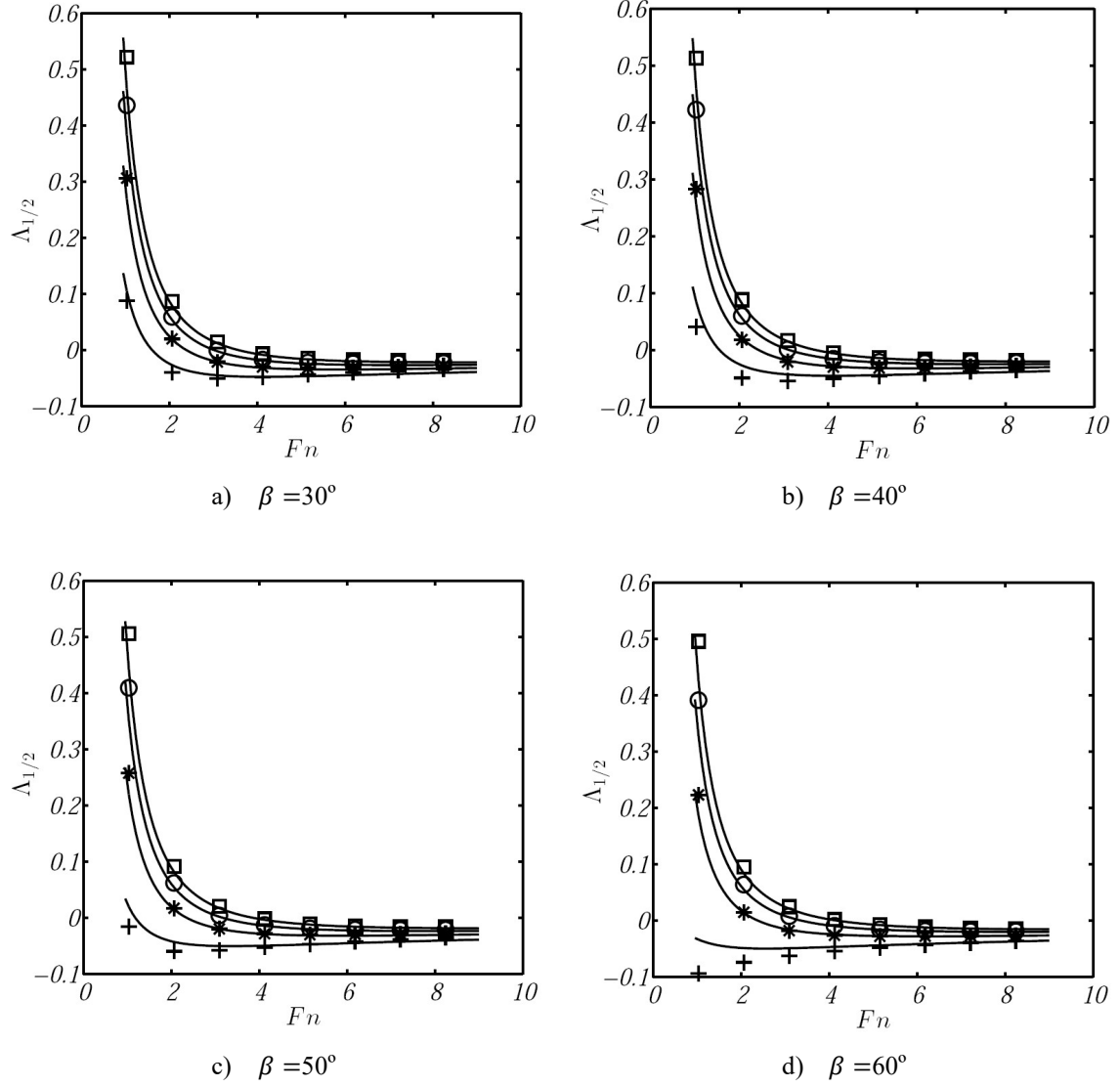
e) $\beta = 30^\circ$

f) $\beta = 40^\circ$

g) $\beta = 50^\circ$

h) $\beta = 60^\circ$
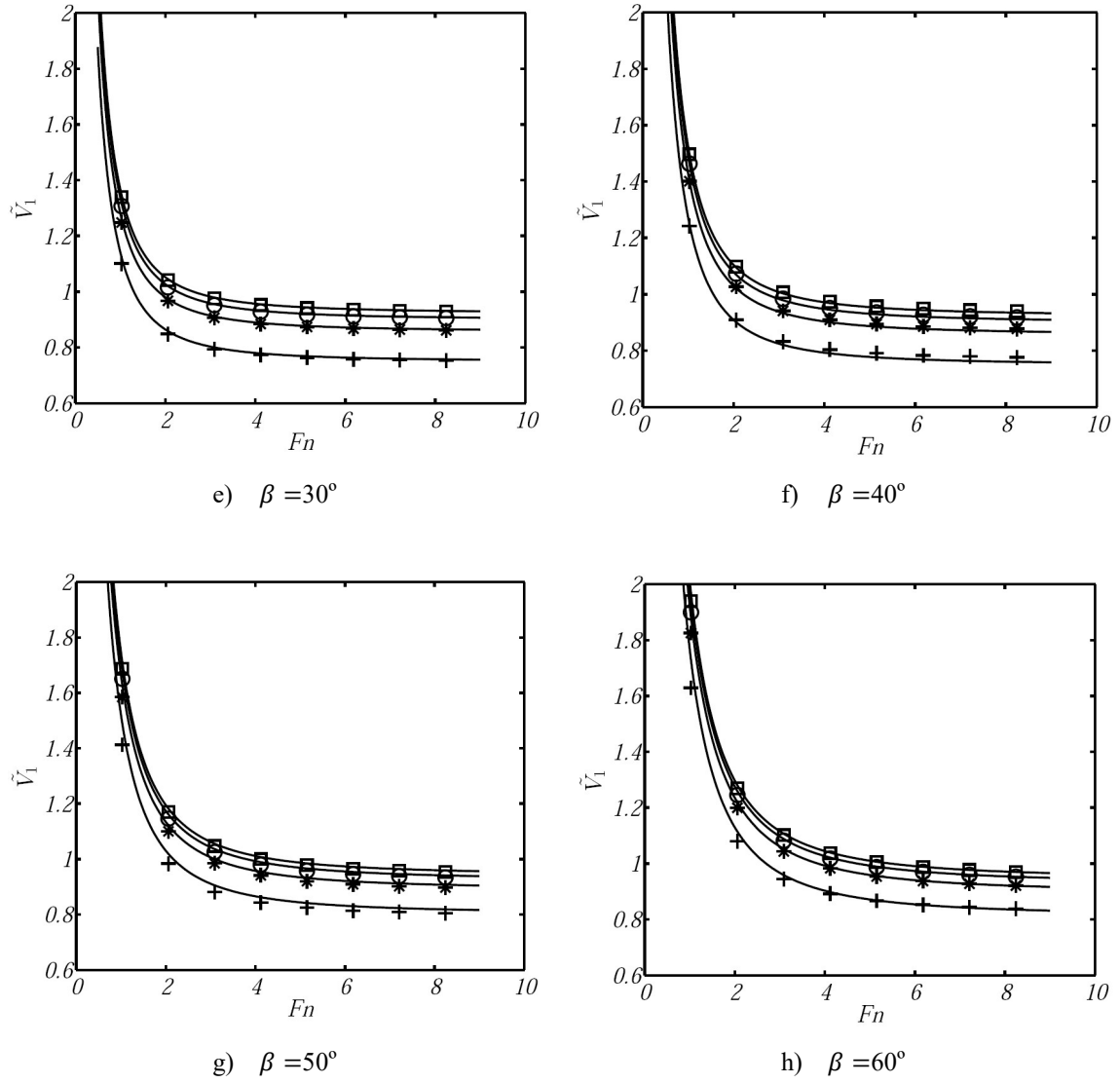
Fig. 3. The peak acceleration of the wedge. The solid lines denote the theoretical predictions. Symbols denote the numerical solution. The results refer to different mass ratios: +, $D_2 = 1/3$; *, $D_2 = 1/6$; O, $D_2 = 1/9$; □, $D_2 = 1/12$. No numerical peak acceleration is observed during the freefall wedge with 60° deadrise angle entering the water surface at $Fn=1$.
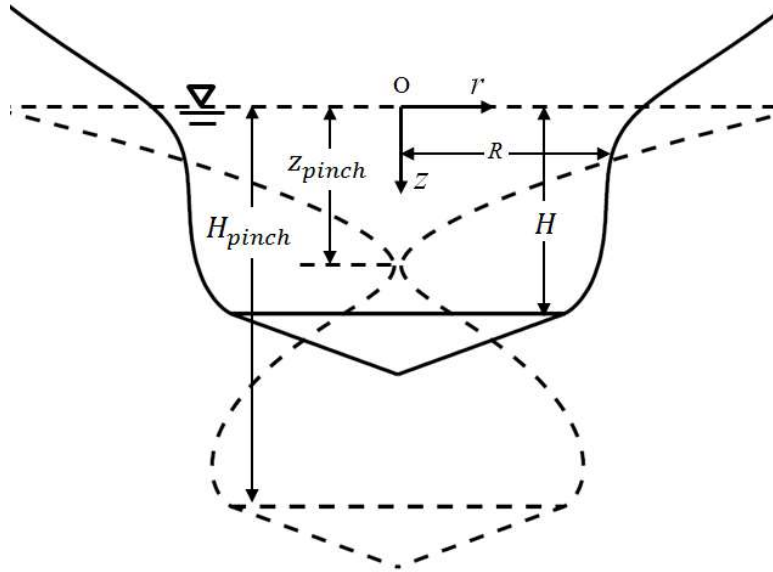
Fig. 4. Coordinate system and symbol definitions for the collapse stage.
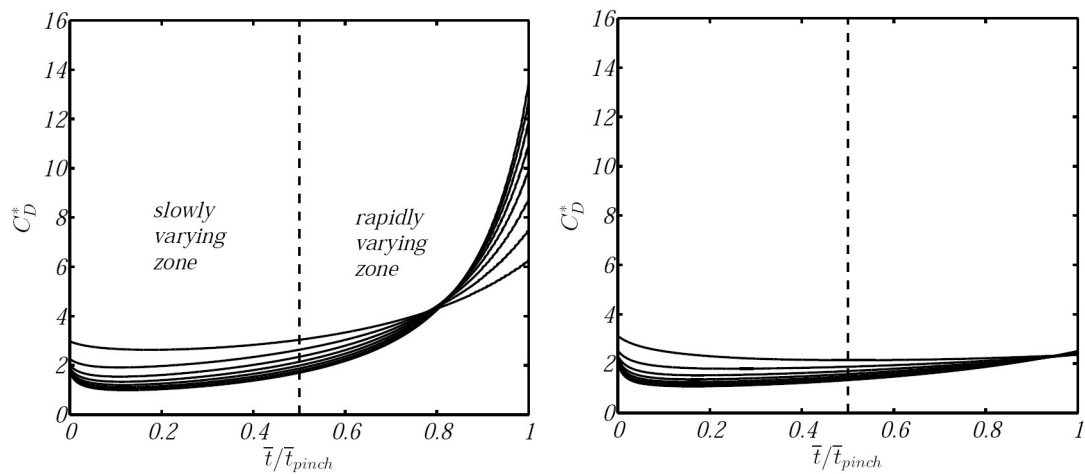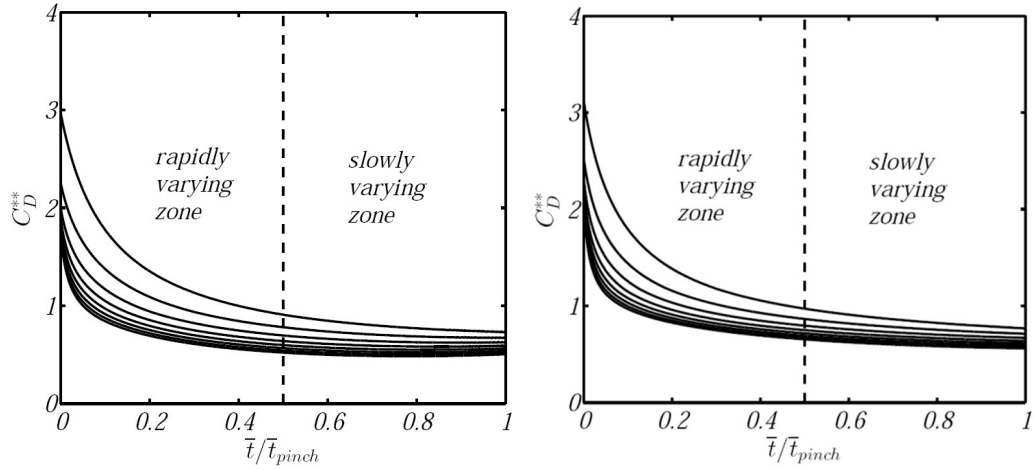

Fig. 5. The time evolution of C_D^* for the wedge of 30° deadrise angle vertically entering into water. The left subfigure corresponds to $D_2 = 1/3$ (the light wedge) and right corresponds to $D_2 = 1/12$ (the heavy wedge). On the first half stage the solid lines from top to bottom correspond to Fn=1, 2, … , 8.
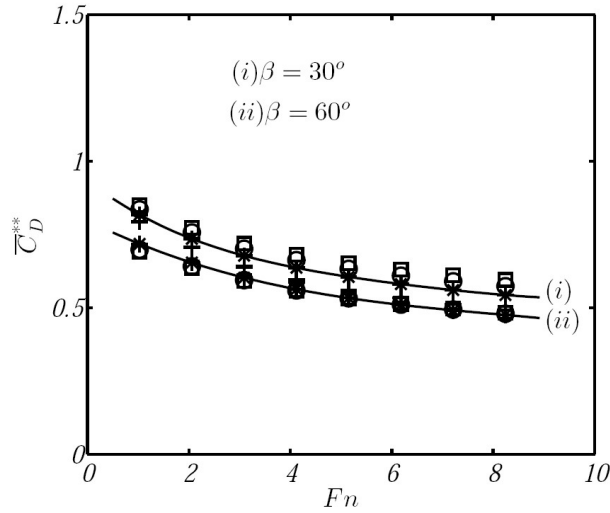
Fig. 6. $\bar{C}_D^*$ against Fn. $\bar{C}_D^*$ is obtained by averaging C_D^* over the first half of the collapse stage. Symbols denote the numerical solution. The results refer to different mass ratios: +, $D_2 = 1/3$; *, $D_2 = 1/6$; O, $D_2 = 1/9$; □, $D_2 = 1/12$. The solid lines denote the fitting of the numerical results of $D_2 = 1/6$ in high-order polynomial.

a) Fn=0.51

b) Fn=1.02

c) Fn=1.92

d) Fn=2.
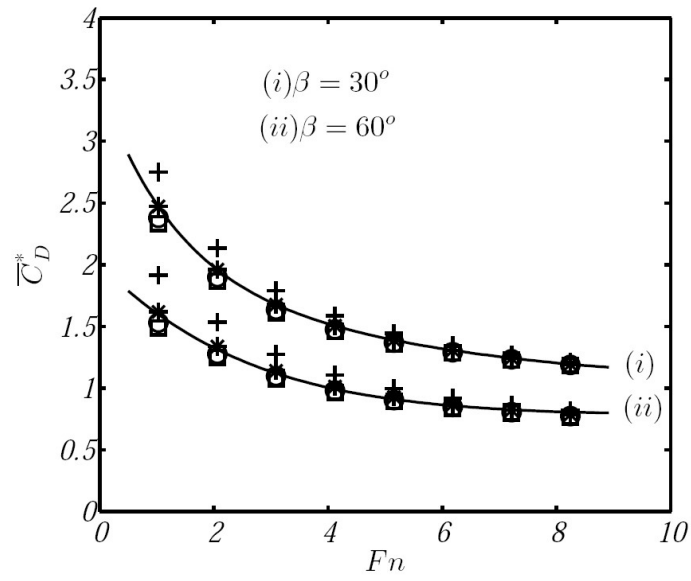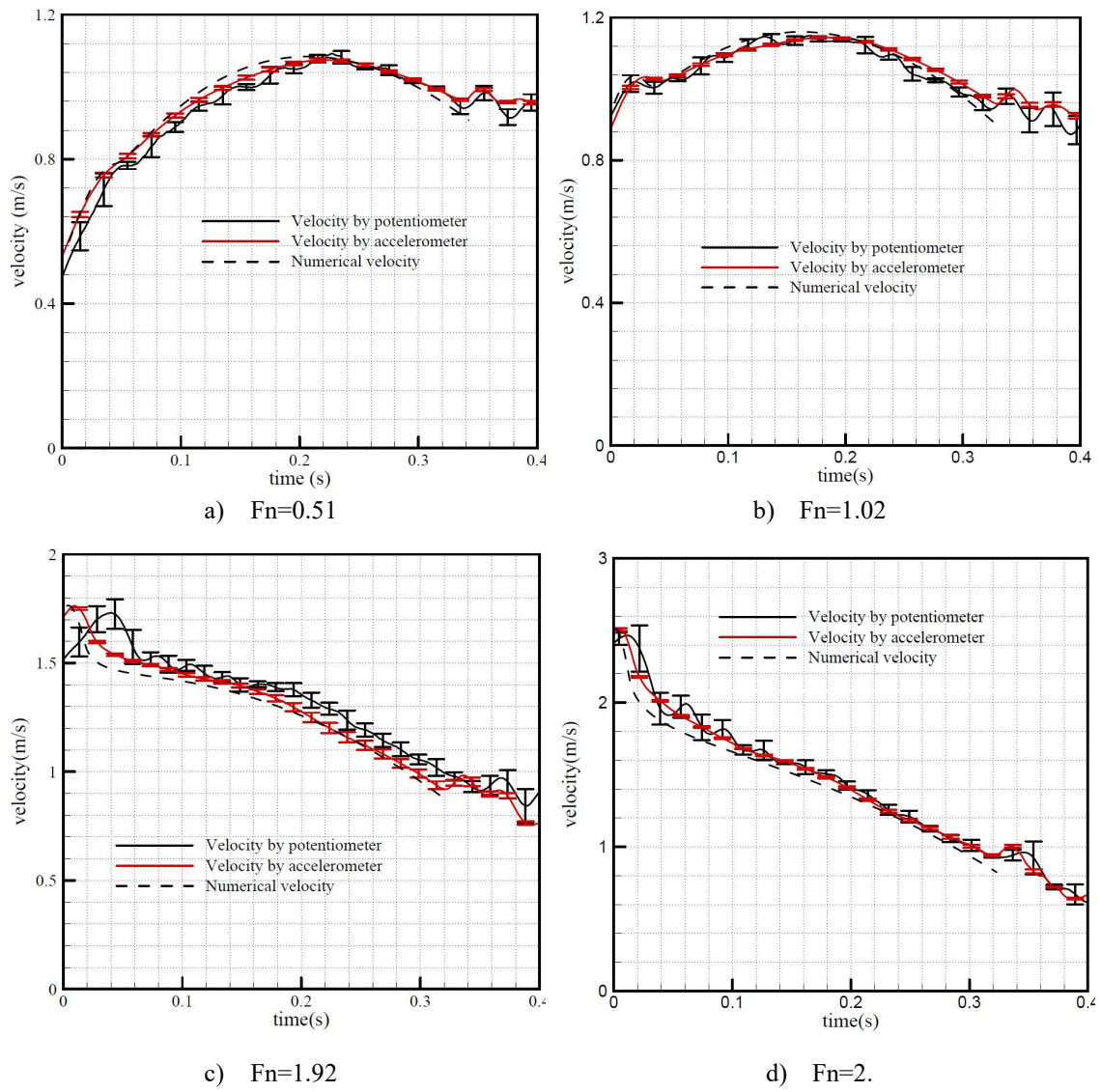
Fig. 7. Evolution of the velocity of the wedge during the water entry of the freefall wedge with a deadrise angle of 30°, c_0=83 mm and $D_2 = 1/3$. The numerical and experimental results refer to [1].
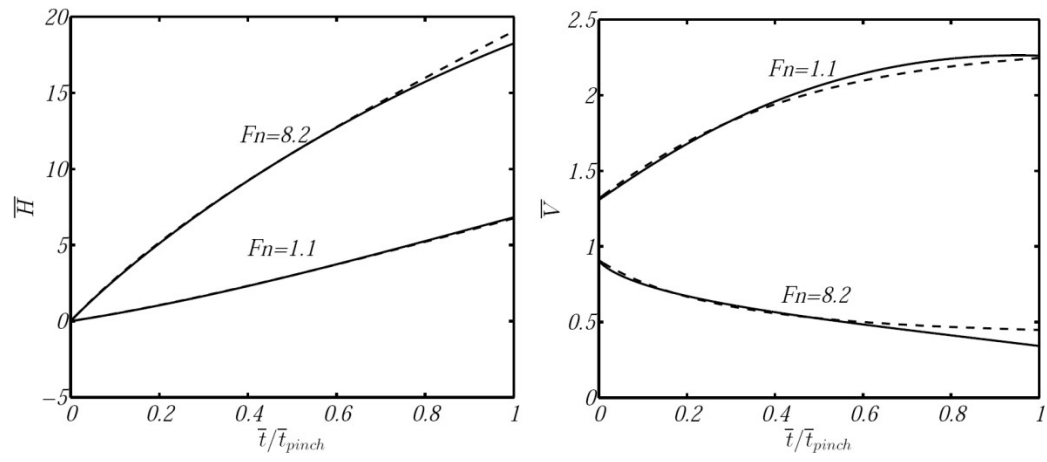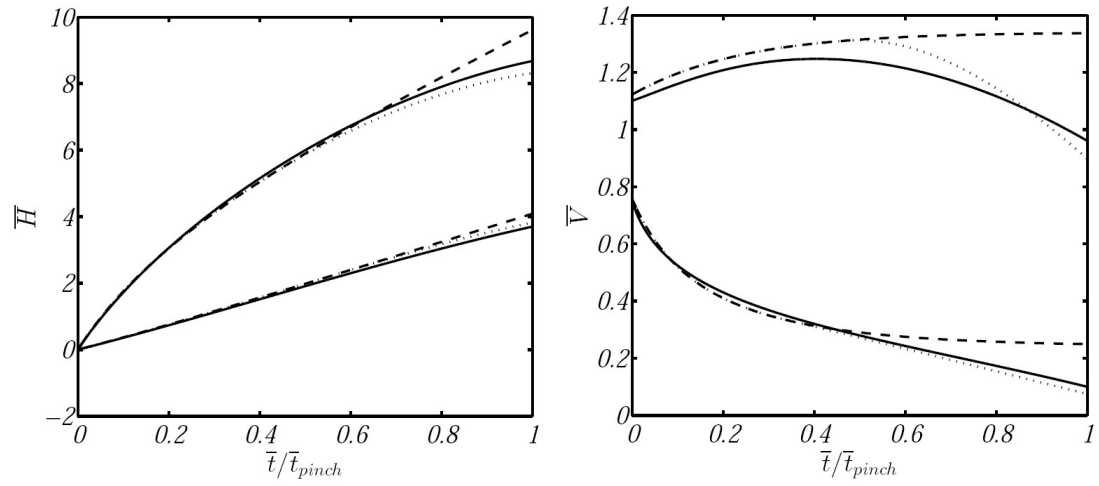
Fig. 8. The time evolutions of the submergence depth and the velocity for the wedge of 30° deadrise angle vertically entering into water. The mass ratio of the wedge is $D_2=1/9$. The solid line represents the numerical results and the dashed line represents the theoretical predictions given by Eqs. (24) and (26).
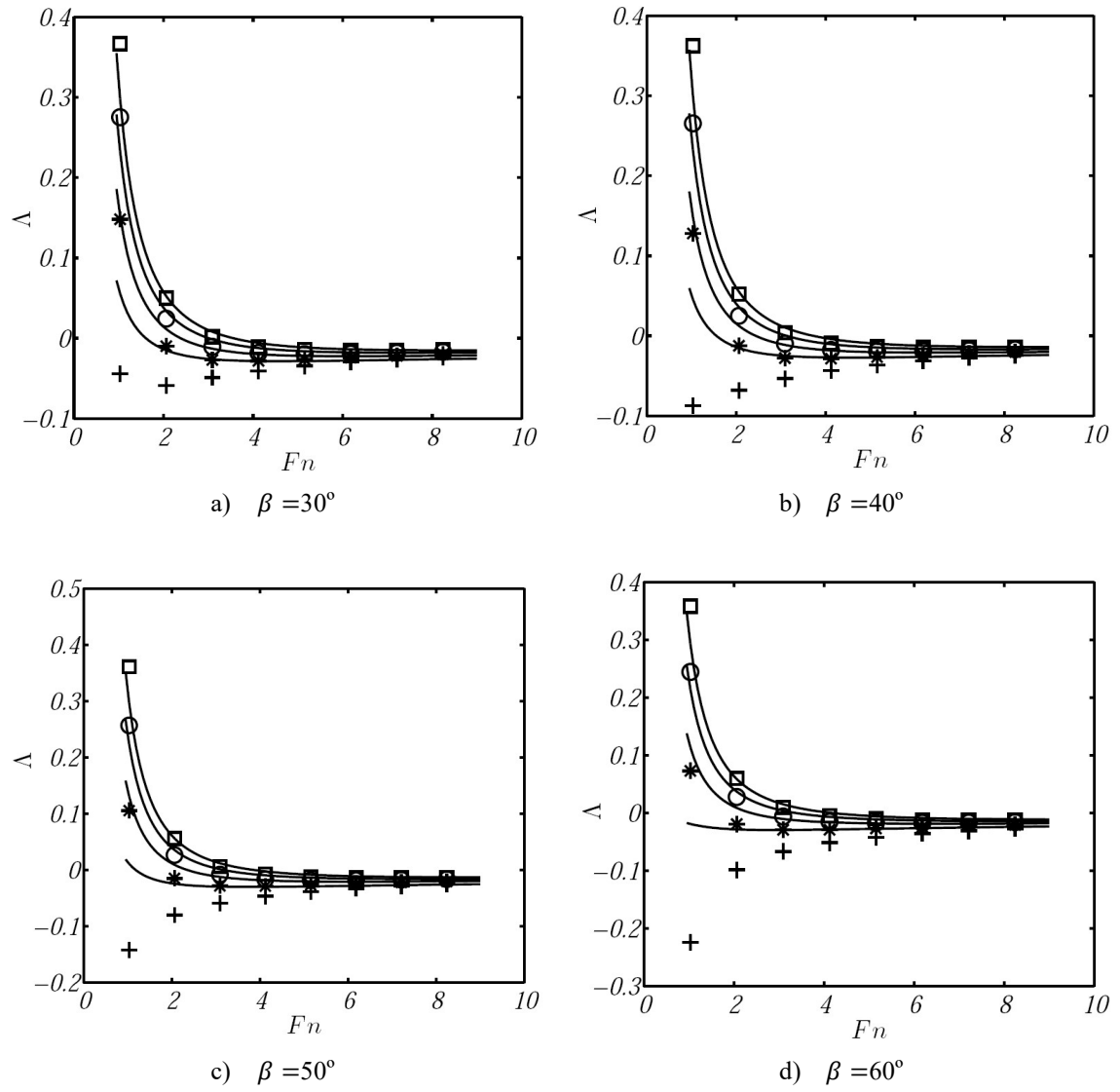
Fig. 9. Dimensionless average accelerations. The solid lines denote the theoretical predictions given by Eq. (29). Symbols denote the numerical solution and the results refer to different mass ratios: +, $D_2=1/3$; *, $D_2=1/6$; O, $D_2=1/9$; □, $D_2=1/12$.

Fig. 10. Dimensionless average accelerations of the first half of the collapse stage. The solid lines denote the theoretical predictions given by Eq. (30). Symbols denote the numerical solution and the results refer to different mass ratios: +, $D_2=1/3$; *, $D_2=1/6$; O, $D_2=1/9$; □ , $D_2=1/12$.

Fig. 11. The time evolution of C_D^{**} for the wedge of 30° deadrise angle vertically entering into water. The left subfigure corresponds to $D_2 = 1/3$ (the light wedge) and right corresponds to $D_2 = 1/12$ (the heavy wedge). On the first half stage the solid lines from top to bottom correspond to Fn=1, 2, … , 8.

Fig. 12. $\bar{C}_D^{**}$ against Fn. $\bar{C}_D^{**}$ is obtained by averaging C_D^{**} over the last half of the collapse stage. Symbols denote the numerical solution. The results refer to different mass ratios: +, $D_2 = 1/3$; *, $D_2 = 1/6$; O, $D_2 = 1/9$; □, $D_2 = 1/12$. The solid lines denote the fitting of the numerical results of $D_2 = 1/6$ in high-order polynomial.

Fig. 13. Time evolutions of the submergence depth and the velocity for the wedge of 30º deadrise angle vertically entering into water. The mass ratio of the wedge is $D_2=1/3$, which represents the light wedge. The solid lines denote the numerical results, the dashed lines the theoretical predictions given by Eqs. (24) and (26), the dot lines the theoretical predictions by matching the solution of Eq. (23) with that of Eq. (33).
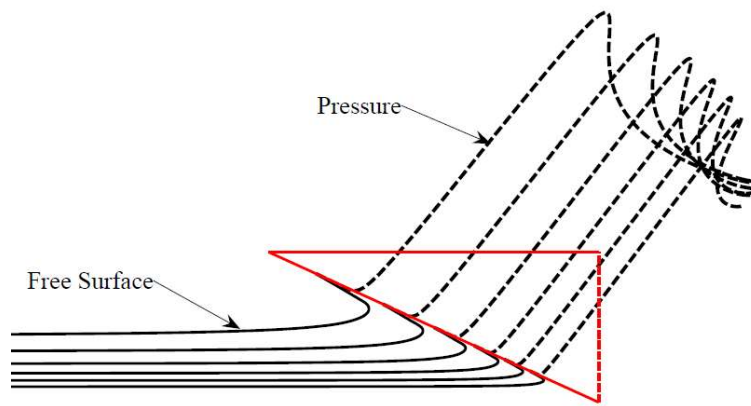
a)
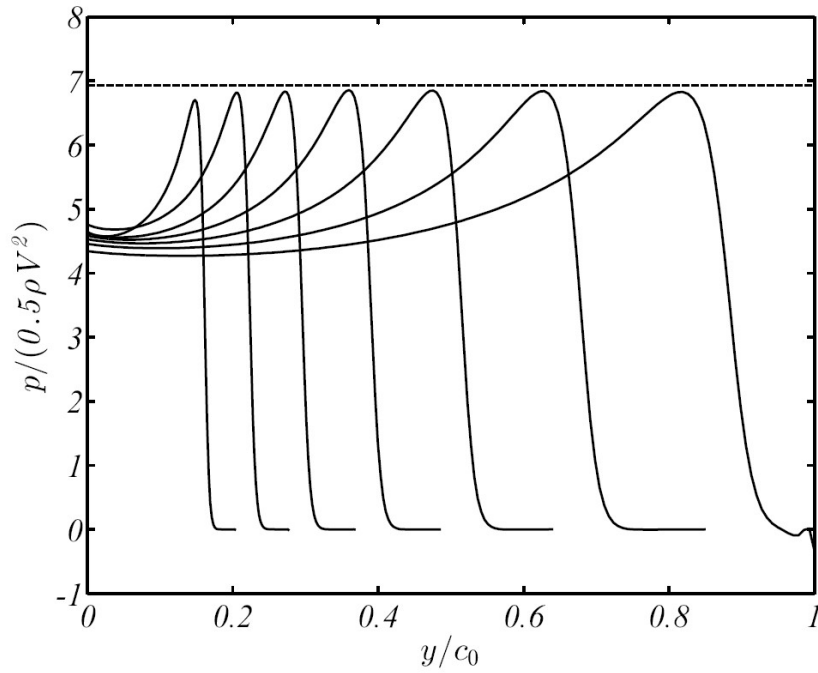
b)

Fig. 14. Evolution of the free surface and the pressure on the impact side before flow separation for the water entry of a freefall wedge with a deadrise angle of 30°, $D_2 = 1/3$, and Fn=1. Subfigure a) shows the evolution of the free surface and pressure. Subfigure b) shows the propagation of the non-dimensional pressure along the impact side: the solid lines denote the pressure distribution; the dashed line denotes the similarity solution of the peak pressure.
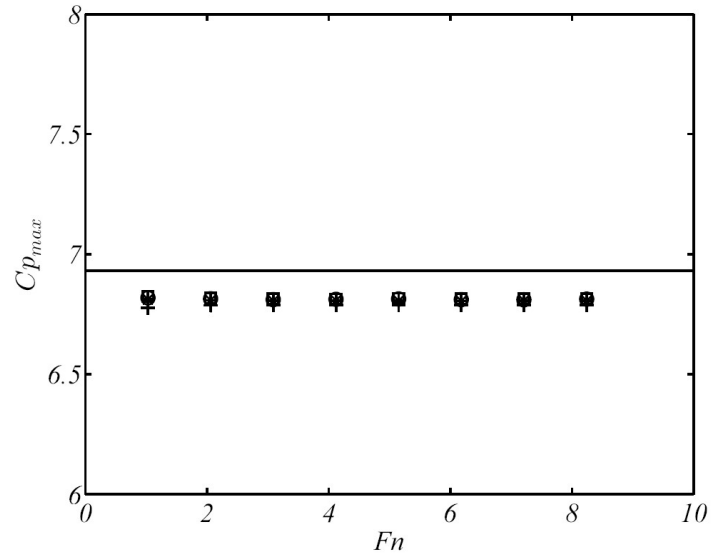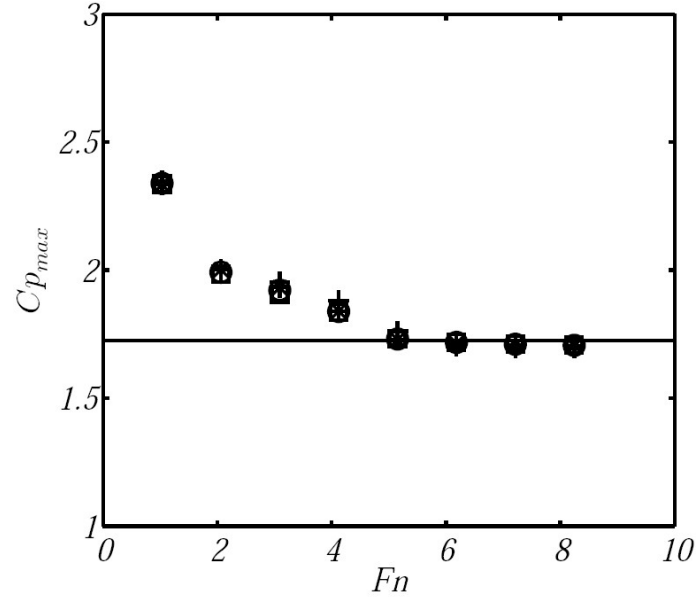
Fig. 15. Coefficients of the peak pressure on the impact side before flow separation for the water entry of a freefall wedge with a deadrise angle of 30°. The solid line denotes the similarity solution. Symbols denote the numerical solution. The results refer to different mass ratios: +, $D_2 = 1/3$; *, $D_2 = 1/6$; O, $D_2 = 1/9$; □, $D_2 = 1/12$.
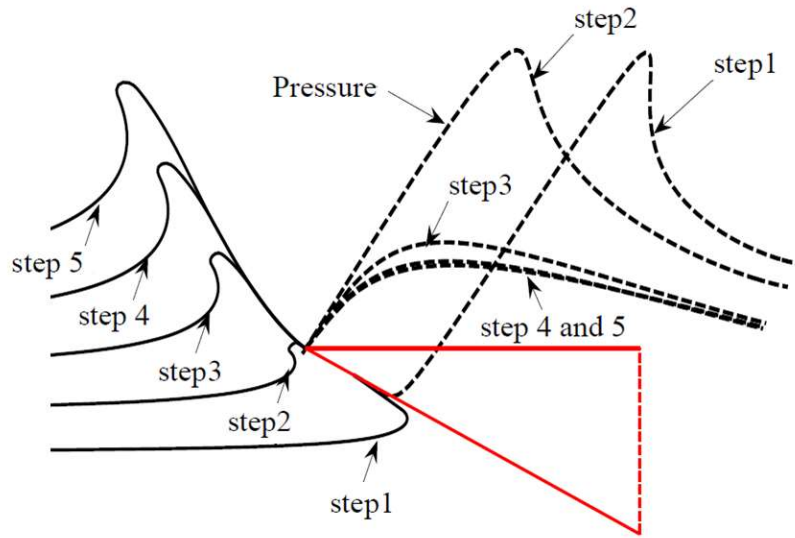
a) slamming stage and transition stage
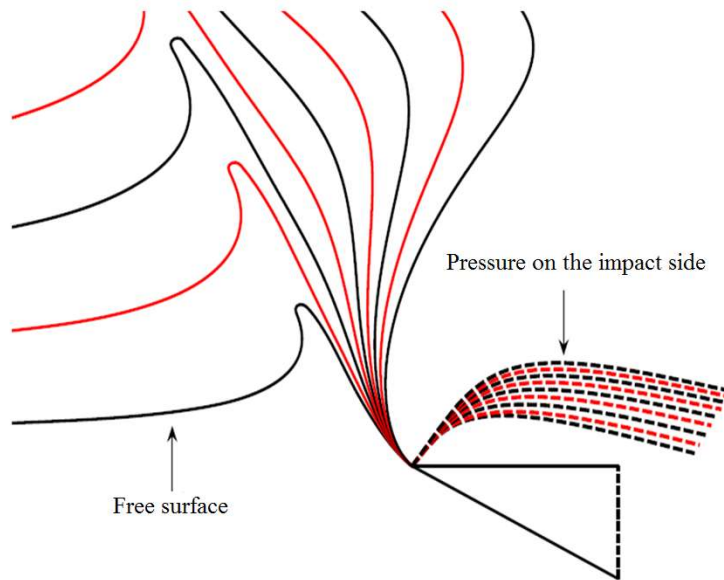
b) collapse stage

Fig. 16. Evolution of the free surface and the pressure on the impact side for the water entry of a freefall wedge with a deadrise angle of 30°, $D_2 = 1/3$, and Fn=1. The coefficient of the peak pressure $Cp_{max} = P_{max}/(0.5\rho V^2)$ of step 1 in the subfigure a) is about 6.8.
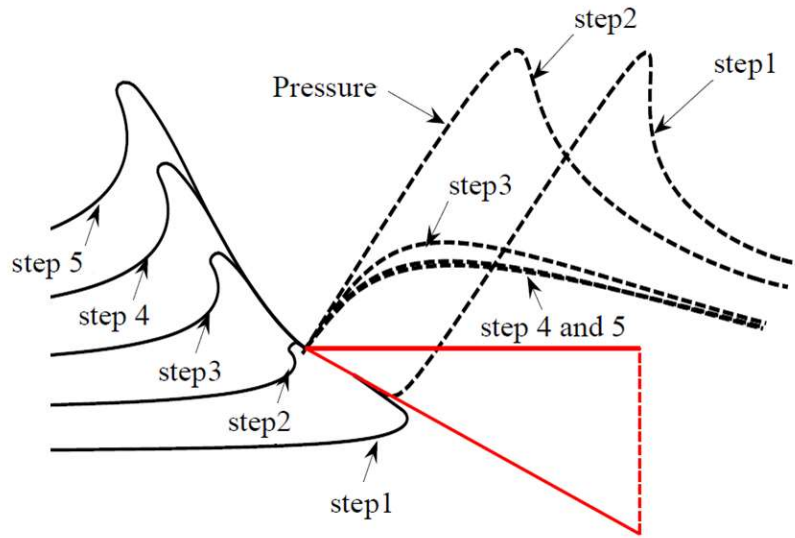
c) slamming stage and transition stage
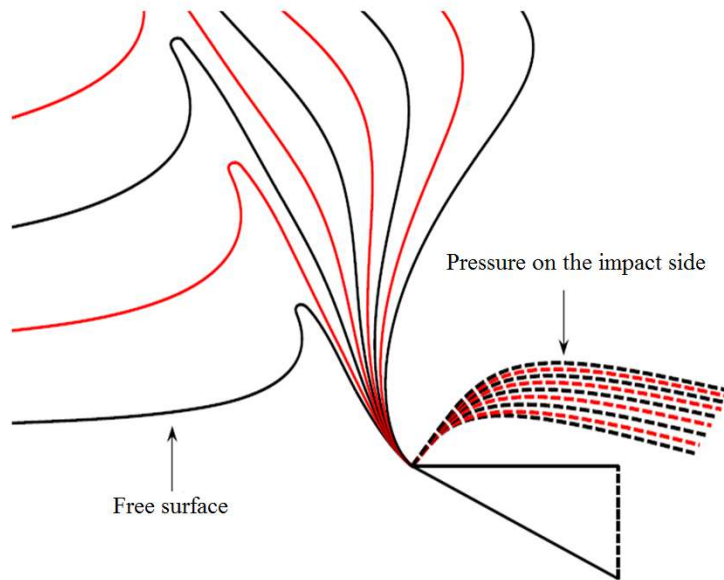
d) collapse stage

Fig. 17. Evolution of the pressure on the impact side for the water entry of a freefall wedge with a deadrise angle of $60°$ and $D_2 = 1/3$. The dashed lines denote the similarity solution of the coefficient of the peak pressure $Cp_{max} = P_{max}/(0.5\rho V^2)$, which is about 1.7 for the deadrise angle of $60°$.

Fig. 18. Coefficients of the peak pressure on the impact side before flow separation for the water entry of a freefall wedge with a deadrise angle of 60°. The solid line denotes the similarity solution. Symbols denote the numerical solution. The results refer to different mass ratios: $+$, $D_2 = 1/3$; $*$, $D_2 = 1/6$; O, $D_2 = 1/9$; $\square$, $D_2 = 1/12$.
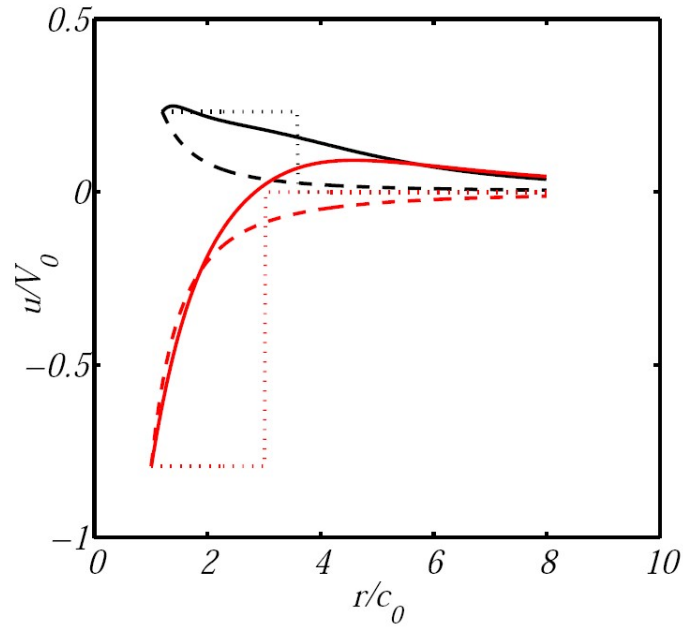

Fig.19. Lateral velocity along the r-axis at the pinch-off depth. The parameters of the freefall wedge correspond to the case 2 of Wang *et al′* s experiments [1]. The numerical pinch-off depth is 0.13 m below the still water surface. The black lines correspond to time=0.2 s, and the red lines time=0.304 s. The solid lines denote the numerical results, the dashed lines the present approximation by using $\eta = 1$, and the dot lines the approximation of the generalized Declaux *et al′* s approach [20].
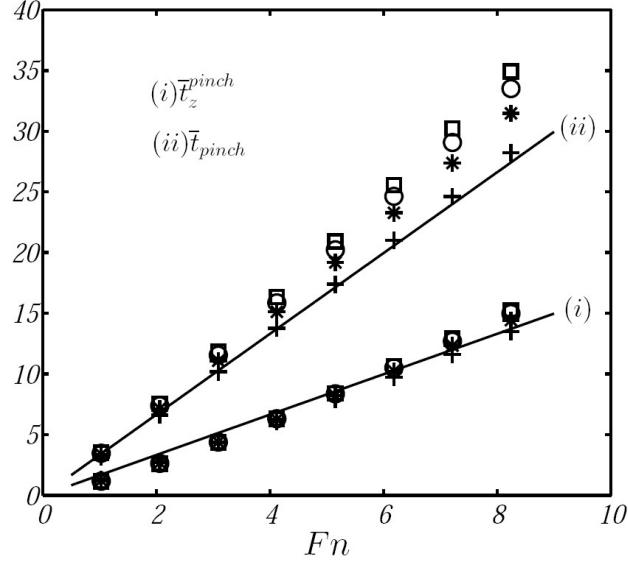
Fig. 20. $\bar{t}_z^{pin}$ and $\bar{t}_{pinch}$ for deadrise angle $\beta = 30^o$. Symbols denote the numerical results for different mass ratios: +, D_2=1/3; *, D_2=1/6; O, D_2=1/9; □, D_2=1/12. The solid lines denote the theoretical prediction given by Eqs. (51)-(52): $\bar{t}_z^{pinc} = 1.6641 * Fn$ and $\bar{t}_{pinch} = 3.3281 * Fn$ (where $\sigma = 1.25$ and $\eta = 1$ are used).
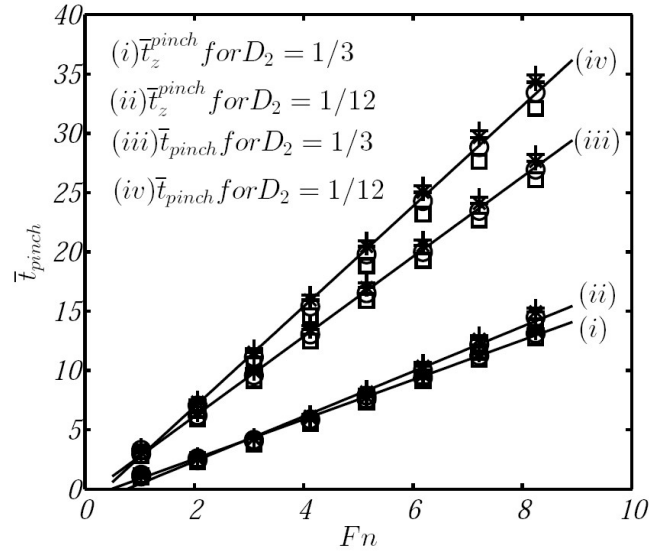

Fig. 21. $\bar{t}_z^{pinch}$ and $\bar{t}_{pin}$ against Fn. Symbols denote the numerical solution. The results refer to different deadrise angles: +, β =30°; *, β =40°; O, β =50°; □, β =60°. The solid lines denote the linear fitting of the numerical results.
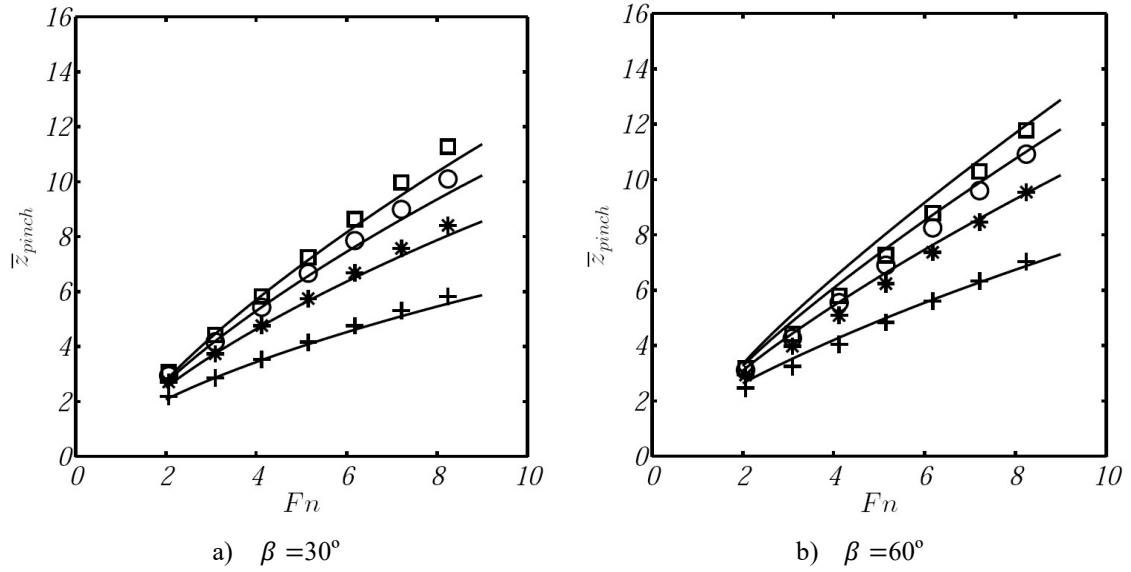
a) $\beta = 30°$

b) $\beta = 60°$

Fig. 22. The pinch-off depth. Symbols denote the numerical results for different mass ratios: +, $D_2 = 1/3$; *, $D_2 = 1/6$; O, $D_2 = 1/9$; □, $D_2 = 1/12$. The solid lines denote the theoretical predictions. Eqs. (53) and (55) are used in the theoretical predictions.

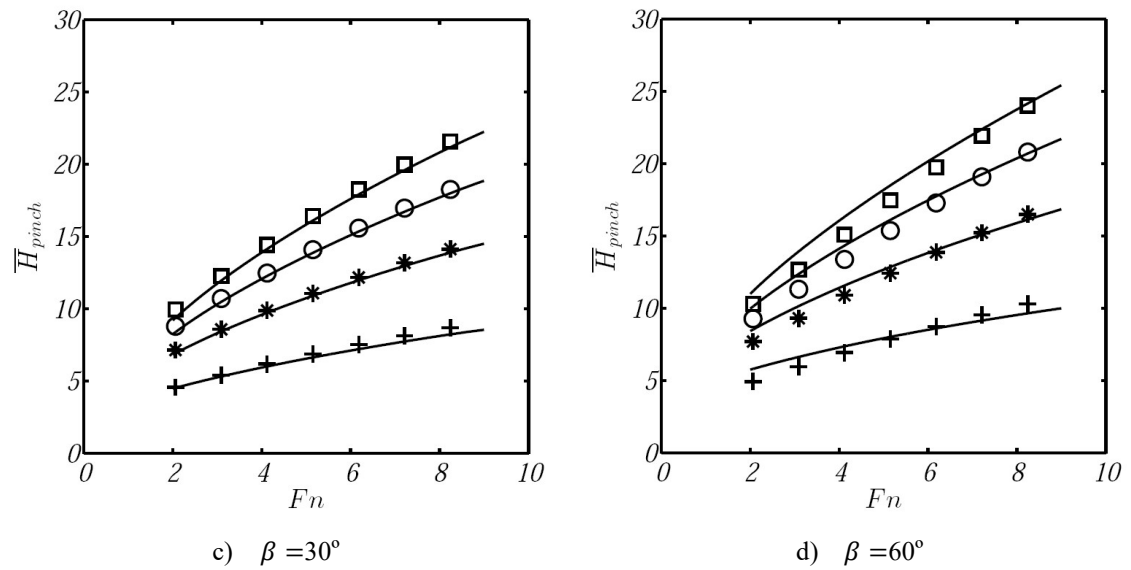c) $\beta = 30°$

d) $\beta = 60°$

Fig. 23. The submergence depth at pinch-off. Symbols denote the numerical results for different mass ratios: +, $D_2 = 1/3$; *, $D_2 = 1/6$; O, $D_2 = 1/9$; □, $D_2 = 1/12$. The solid lines denote the theoretical predictions. Eqs. (54) and (56) are used in the theoretical predictions.